



COMPUTATIONAL ANALYSIS OF GEOMETRIC EFFECTS
ON STRUT INDUCED MIXING IN A SCRAMJET
COMBUSTOR

THESIS

Matthew G. Bagg, Captain, USAF

AFIT/GAE/ENY/09-M01

DEPARTMENT OF THE AIR FORCE
AIR UNIVERSITY

AIR FORCE INSTITUTE OF TECHNOLOGY

Wright-Patterson Air Force Base, Ohio

APPROVED FOR PUBLIC RELEASE; DISTRIBUTION UNLIMITED.

The views expressed in this thesis are those of the author and do not reflect the official policy or position of the United States Air Force, Department of Defense, or the United States Government.

AFIT/GAE/ENY/09-M01

COMPUTATIONAL ANALYSIS OF GEOMETRIC EFFECTS ON STRUT
INDUCED MIXING IN A SCRAMJET COMBUSTOR

THESIS

Presented to the Faculty

Department of Aeronautical and Astronautical Engineering

Graduate School of Engineering and Management

Air Force Institute of Technology

Air University

Air Education and Training Command

In Partial Fulfillment of the Requirements for the
Degree of Master of Science in Aeronautical Engineering

Matthew G. Bagg, BS

Captain, USAF

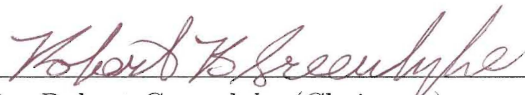
March 2009

APPROVED FOR PUBLIC RELEASE; DISTRIBUTION UNLIMITED.

COMPUTATIONAL ANALYSIS OF GEOMETRIC EFFECTS ON STRUT
INDUCED MIXING IN A SCRAMJET COMBUSTOR


Matthew G. Bagg, BS
Captain, USAF

Approved:




Dr. Robert Greendyke (Chairman)

18 Mar 09
Date



Dr. Paul King (Member)

18 Mar 09
Date



Maj. Andrew Lofthouse (Member)

18 Mar 09
Date

Abstract

In order to increase the fuel-air mixing in a scramjet combustion section, the Air Force Institute of Technology and the Air Force Research lab investigated methods to increase the mixing efficiency. Previous experimental work identified the advantages of using a strut upstream of a cavity flame holder to increase the fuel-air mixture. In this paper a computational investigation of strut injectors in a supersonic flow with a cavity flame holder is reported. This research focused on understanding the effect of a change in height and width of the strut upstream of the combustion cavity on the mixing efficiency and pressure loss in the combustion section. Three baseline struts from the previous experimental research had slightly different trailing edge designs; a flat trailing edge, a 45 degree slanted trailing edge and a 6.45 cm extension. Twelve more struts were made from the baselines struts by varying the height and width by 50% of the baseline value. Computational simulations were conducted on all fifteen struts using the VULCAN computational fluid dynamics solver. Struts with a height or width increased from the baseline value exhibited an increase in the total pressure loss through the combustion section. This total pressure loss correlated to the larger low pressure region created by the flow displacement caused by the strut. The struts evaluated with decreased height and width showed a lower total pressure loss since they produced a smaller low pressure region in the wake. The low pressure region is key to the mixing caused by the struts. The larger struts caused a larger combustible area in the combustion section while the small struts produced a smaller combustible area. The size of the strut becomes a key design tradeoff between increased mixing and total loss performance.

Acknowledgements

I would like to thank Dr. Dean Eklund, Dr. Mark Gruber, Dr. Mark Hsu and Dr. John Tam of the Air Force Research Lab Propulsion Directorate for funding this research. All four provide valuable guidance in understanding the initial AFRL research, grid generation and use of the VULCAN CFD solver. Dr. Jeff White of NASA also aided in the understanding of how VULCAN worked.

Thanks to my advisor, Dr. Robert Greendyke, and the rest of the AFIT faculty for imparting their wisdom and knowledge to me during my time here.

A special thank you goes to my family and friends for their support and understanding during my time at AFIT.

Matthew G. Bagg

Table of Contents

	Page
Abstract	iv
Acknowledgements	v
List of Figures	viii
List of Tables	x
List of Symbols	xi
List of Abbreviations	xiii
I. Introduction	1
II. Background	4
2.1 Parallel, Normal and Transverse Injection	5
2.2 Ramps	6
2.3 Struts	8
2.4 Current Research	10
III. Computational Setup	12
3.1 Computational Domain	12
3.1.1 Struts	12
3.1.2 Inflow Conditions	14
3.2 VULCAN Code	17
3.2.1 Laminar and Turbulent	17
3.2.2 Non-reacting flow	19
3.2.3 Steady Flow	19
3.2.4 Flux Scheme	19
3.2.5 Convergence Criteria	20
3.3 Grid Generation	20
3.4 Data Collection	23
3.4.1 Total Pressure Loss	24
3.4.2 Equivalence Ratio	26
IV. Results and Discussion	29
4.1 Total Pressure Loss	29
4.1.1 Laminar	30
4.1.2 Turbulent Results	31
4.2 Combustible Area	46
4.2.1 Laminar	46

	Page
4.2.2 Turbulent	47
4.3 Flame Comparison	49
V. Conclusions	53
5.1 Impact	55
5.2 Future Work	56
Bibliography	57
Vita	59

List of Figures

Figure		Page
2.1	Range of operation of different engine designs [5]	4
2.2	Basic scramjet layout	5
2.3	Parallel fuel injection	5
2.4	Normal fuel injection [9]	6
2.5	Ramps used for mixing [11]	7
2.6	Strut used in Ref [12]	8
2.7	Alternating Wedge strut used in Ref [13]	9
2.8	Diagram of basic strut from Ref [16]	10
2.9	Image of struts used in AFRL research [4]	11
3.1	Side view of computational domain	13
3.2	Dimensions of the cavity	14
3.3	The three baseline struts	14
3.4	Comparison of different strut 1 sizes	15
3.5	Comparison of different strut 2 sizes	15
3.6	Size comparison for strut 3	16
3.7	Location and direction of injectors	18
3.8	Views of grid	21
3.9	View of domains on side of Strut S1B	22
3.10	Injector domains on side of Strut S1B	23
3.11	Top view of domains on Strut S1B	23
3.12	Domain configuration in the cavity	24
3.13	Planes used for data collection	25
4.1	Side view of velocity vectors behind strut	30
4.2	Top view of velocity vectors behind strut	31
4.3	Laminar combustion section exit pressure contours	32
4.4	Turbulent total pressure contours for S1 at combustion section exit	34

Figure		Page
4.5	Velocity Profiles at different locations after S1B	35
4.6	Velocity vectors seen in previous research [20]	36
4.7	Velocity Profiles at different locations after S1H1	37
4.8	Velocity Profiles at different locations after S1H2	38
4.9	Velocity Profiles at different locations after S1W1	40
4.10	Velocity Profiles at different locations following S1W2	41
4.11	Streamlines to identify source of low pressure lobes	42
4.12	Velocity Profiles at two locations following S2B	43
4.13	Velocity Profiles at two locations following S2H2	44
4.14	Velocity Profiles at two locations following S2W2	45
4.15	Velocity Profiles at two locations following S3B	46
4.16	Laminar equivalence Ratio at three stations behind the strut . . .	48
4.17	Equivalence ratio at three stations behind strut S1	50
4.18	Flame location for S1B	51
4.19	Flame location for S2B	52
4.20	Flame location for S3B	52

List of Tables

Table		Page
3.1	Inlet Conditions	17
4.1	Laminar total pressure ratio across combustion section	32
4.2	Turbulent total pressure loss for S1	33
4.3	Preliminary turbulent total pressure loss for S2	43
4.4	Preliminary turbulent total pressure loss for S3	45
4.5	Combustion area (cm ²) at three locations behind the strut	47
4.6	Combustion area (cm ²) at three locations behind S1	49
4.7	Preliminary Combustion area (cm ²) for S2 and S3B	49

List of Symbols

Symbol		Page
S1B	Strut 1 Baseline	12
S2B	Strut 2 Baseline	12
S3B	Strut 3 Baseline	13
S2H2	Strut 2 Tall	13
O ₂	Oxygen	14
N ₂	Nitrogen	14
C ₂ H ₄	Ethylene	16
\dot{M}_{error}	Mass flow rate error	20
\dot{M}_{in}	Mass flow rate into the domain (kg/s)	20
\dot{M}_{out}	Mass flow rate out of the domain (kg/s)	20
Y ⁺	Non-Dimensional Wall Distance	20
u_*	Friction velocity (m/s)	21
y	Distance to the wall (m)	21
ν	Kinematic viscosity (m ² /s)	21
P	Total pressure (Pa)	24
Φ	Equivalence Ratio	26
m_{fuel}	Mass of fuel (kg)	26
m_{air}	Mass of Air (kg)	26
st	Stoichiometric Conditions	26
Y	Mass fraction	26
m_{total}	Total Mass (kg)	26
S1H2	Strut 1 Tall	30
S1W2	Strut 1 wide	30
S1H1	Strut 1 short	31
S1W1	Strut 1 thin	31
S2W2	Strut 2 wide	42

Symbol		Page
S2H1	Strut 2 short	43
S2W1	Strut 2 thin	43
S3H1	Strut 3 short	45
S3H2	Strut 3 tall	45
S3W1	Strut 3 thin	45
S3W2	Strut 3 wide	45

List of Abbreviations

Abbreviation		Page
Scramjet	Supersonic combustion Ramjet	1
USAF	United States Air Force	1
NASA	National Aeronautics and Space Administration	1
AFRL	Air Force Research Laboratory	2
RZ	Propulsion Directorate	2
CFD	Computational Fluid Dynamics	16
VULCAN	Viscous Upwind Algorithm for Complex Flow Analysis	17
LDFSSB	Blended Low Dissipation/van Leer Flux Splitting Scheme	17
LDFSS	Low Dissipation Flux Splitting Scheme	19

COMPUTATIONAL ANALYSIS OF GEOMETRIC EFFECTS ON STRUT INDUCED MIXING IN A SCRAMJET COMBUSTOR

I. Introduction

Recent emphasis on the capability of rapid access to space has caused an increased interest in the development of enhanced propulsion capabilities for Scramjet engines. Scramjet engines are a necessary component for the proposed class of reusable hypersonic vehicles necessary to undertake any rapid deployment to space. Much research (both experimental and computational) has already taken place in this field however there is still room for improving the performance of this class of engines.

In 1958, work done at the Brooklyn Polytechnic Institute proved that steady combustion was achieved in a flow with a Mach number of 3.0. This discovery led to research in Supersonic Combustion Ramjet (Scramjet) started in the early 1960s and sponsored by the U.S. Air Force (USAF), National Aeronautics and Space Administration (NASA), and the U.S. Navy to support a single stage to orbit space plane and hypersonic cruise missiles. This research was also fueled by increased interest and funding of space related studies at the time [1]. Unfortunately, most of these endeavors were limited to ground test only due to complications in design and strict time tables. These ground tests did result in proving the possibility of hypersonic flight showing high thrust performance, reaching 70% of ideal performance and displayed the use of a scramjet in the Mach number range of 5-7 [2]. The ground tests also supplied a wealth of knowledge to further the development of scramjet engines [3].

A joint undertaking occurred in the mid 1980s initiated by the Defense Advanced Research Projects Agency (DARPA) that renewed interest in scramjet engines. The program's aim was to develop a single stage to orbit plane named the National Aerospace Plane (NASP). This project became a joint venture including the USAF, NASA, U. S. Navy and several engine and airframe development companies.

As with previous programs, this program encountered budget cuts and high technical risk which lead to it being cancelled in the mid 1990s. NASA was able to keep part of the NASP program going and developed the Hyper-X vehicle which completed flight tests in 2004 at a Mach number of 6.8 and 9.6.

NASA's Hyper-X vehicle used hydrogen fuel for combustion however the USAF is more interested in using hydrocarbon fuel in a scramjet engine. While hydrogen is the preferred fuel for space launch applications due to the increased energy released and quicker burn time, hydrocarbon fuel is better suited for air-launch missiles and smaller aircraft and favored by the USAF. Using hydrocarbon fuel could also allow the USAF to use existing aircraft fuel and reduce the logistical complexity of the system. Hydrocarbon fuels also require less space than hydrogen leading to smaller and perhaps stealthier vehicles. Current test facilities are capable of testing the full range of Mach numbers for hydrocarbon fueled scramjet engines.

The Air Force Research Laboratory (AFRL) has been conducting research into hydrocarbon fueled scramjets in recent years. Most of this research is supported by the Propulsion Directorate (RZ) and includes both experimental and computational programs. The primary goal of this research is to evaluate and develop fuel injection processes and methods to increase the efficiency of the combustion in a hydrocarbon fueled scramjet. Improving the fuel injection techniques allows for the smaller scale test done in the lab to be expanded to a usable scramjet for real world applications. One of the fuel injection and mixing techniques evaluated at AFRL [4] was the use of three different struts for fuel injection and mixing in conjunction with a cavity flame holder. The results from this research showed an increase in mixing and combustion in the combustion section of a scramjet caused by the struts. The research sparked further study of the strut geometry used.

The objective of this research is to assess the mixing efficiency and total pressure loss of 15 strut designs based on the struts used by AFRL. The strut design allows the hydrocarbon fuel to be injected normal to the supersonic airflow, which causes mixing

of the fuel and air to a sufficient ratio for combustion. Twelve new strut designs are variations of the height and width of the three struts used in the AFRL research, bringing the total to 15 struts to be examined. Specific performance measurements used to compare all 15 strut designs include the equivalence ratio and total pressure loss. The results of this research could lead to more efficient strut designs that would create shorter supersonic combustion sections than are currently available. A shorter combustion section means a smaller and lighter scramjet engine to be used in real world applications.

II. Background

A scramjet engine is capable of operating in a speed regime of Mach numbers from 4-16, which turbojet engine technology can not reach. This regime is typically where rocket engines are used, but a scramjet provides superior specific impulse and is not required to carry the oxidizer onboard. A comparison of the range of operation for different engines is displayed in Figure 2.1 [5]. For a hydrocarbon fueled scramjet, the maximum speed is limited to a Mach number of 9 [6].

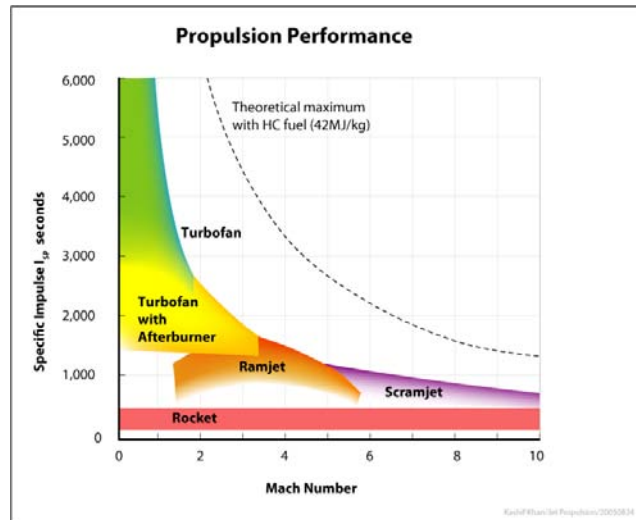


Figure 2.1: Range of operation of different engine designs [5]

A scramjet engine consists of three main components, a converging inlet, a supersonic combustor, and a divergent nozzle as shown in Figure 2.2. The inlet takes the high velocity freestream flow, at a Mach number of 4 or higher, and compresses it through a series of shocks to a Mach number of 1-3. The flow then enters the combustion section where fuel is injected, mixed and ignited to produce the thrust of the engine. The flow is accelerated and exits the engine through the nozzle. The primary issue in a scramjet is the supersonic combustion process, which leads to the fuel injection and mixing to be the focus of most supersonic combustion research.

Supersonic combustion is difficult because the engine is required to mix and burn the fuel before the fuel leaves the nozzle of the engine. One way to solve this problem is to make the combustion section long so that the fuel has enough time to

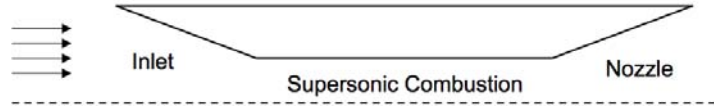


Figure 2.2: Basic scramjet layout

mix with the air and produce thrust. This solution is only useful in the laboratory environment since the test devices are usually scale models of a real scramjet. However, a long combustion section does not scale well to be used on a missile or vehicle. A large combustion section would make the engine heavier and impact the weight of an air vehicle on which the engine is installed. To reduced the size of the combustion section, and the size of the scramjet engine, various mixing techniques were evaluated to identify which ones improved the mixing while having the least effect on the performance of the engine.

2.1 *Parallel, Normal and Transverse Injection*

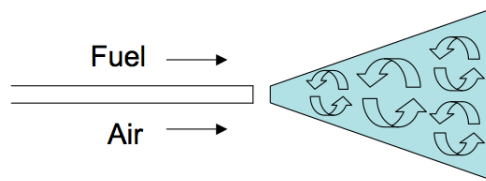


Figure 2.3: Parallel fuel injection

Early scramjet research focused on either parallel or normal fuel injection in relation to the main flow of the engine to create mixing areas just upstream of the combustion. As in Figure 2.3, parallel fuel injection consists of fuel flowing parallel to the air in the engine but separated by a splitter plate. When the splitter plate ends, a shear layer is created due to the different velocities of the fuel and air. The shear layer is the primary source of mixing the fuel with the air so that proper combustion can be achieved. When parallel fuel injection was tested with a hydrogen-fluorine fuel in air, the growth rate of the shear layer was reduced compared to theoretical rates. The reduction in growth rate is argued to be caused by the reduction of turbulent

shear stress at the core of the shear layer due to the density change caused by the heat released from the combustion process. [7, 8].

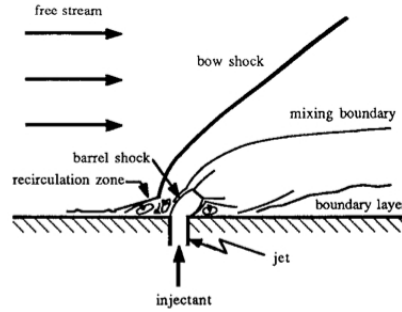


Figure 2.4: Normal fuel injection [9]

Normal fuel injection consists of an injection port on the wall of a scramjet. The port injects the fuel normal to the flow of air in the scramjet. Normal fuel injection creates a detached normal shock upstream of the injector which causes separation zones upstream and downstream of the injector as in Figure 2.4. The separation zones cause increased total pressure losses which affect the efficiency of the engine. However, the downstream separation regions can be used as a flame holder. Research conducted to minimize the total pressure loss displayed low combustion efficiency due to poor mixing [9].

Transverse fuel injection is a combination of parallel and normal fuel injection. In a transverse injector, the fuel is injected at an angle between normal and parallel to the flow. Transverse injection reduces some of the negatives to normal injection, but requires a larger injection pressure to achieve the same penetration height into the air flow. The increase in the injection pressure increases the total pressure loss of the scramjet which decreases the efficiency of the engine. Since these injection techniques do not meet the needs in a scramjet, more complex mixing methods were evaluated.

2.2 Ramps

Using the results from parallel injection, it was theorized [10] that adding axial velocity to the parallel injection may increase the mixing. To add axial velocity to

the flow near fuel injection, ramps were added with fuel injectors on the trailing edge of the ramp injecting fuel parallel to the flow. The flow over the ramps created counter-rotating vortices that increased the mixing. Due to the supersonic flow in the scramjet, the ramps also create shocks and expansion fans which cause pressure gradients that also increase mixing. Two types of ramps were used; compression ramps are elevated above the floor while expansion ramps create troughs in the floor (Figure 2.5).

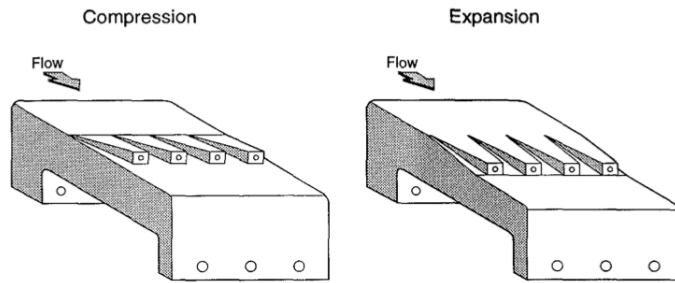


Figure 2.5: Ramps used for mixing [11]

Research compared several different compression and expansion ramp geometries [11]. The shock formation in the ramps depended on the type. In compression ramps the shocks formed at the base of the ramp and in expansion ramps the shocks formed in the recompression region at the bottom of the trough. Due to the difference in the shock locations, the combustion efficiency and mixing for the two ramp styles differed. The results showed that compressor ramps created a stronger vortex and increased the fuel/air mixing, but expansion ramps had the higher combustion efficiency. Combustion efficiency requires mixing at the smaller scales that the expansion ramps provide, and the strong vortex generated by the compression ramps degrades the small scale mixing. Another interesting result was that the expansion ramps reached their maximum combustion efficiency in less distance than compression ramps, which would allow for shorter combustion sections and thereby minimizing weight.

While ramps did improve the mixing caused by parallel injection, the ramps are placed along the wall of the combustion section which limited the fuel penetration

into the combustion section. In order to achieve penetration throughout the flow field, a more intrusive method was required.

2.3 Struts

Research into strut mixing devices covers a wide range of designs and includes both normal and parallel injection methodologies. Most struts consist of a vertical strut with a wedge leading edge. The strut is connected to both the bottom and top of the combustion section. Since it is across the whole combustion section, fuel injection occurs at several locations and allows the fuel to be added throughout the flow field. Research [12] compared three mixing techniques for scramjet combustion: transverse injection in a cavity, two-stage normal and transverse injection, and a strut consisting of a vertical wedge front with fuel injection in the back side of the trailing edge as seen in Figure 2.6. Results showed that a strut was the only technique that affected the entire flow field but had a higher pressure loss than the other techniques. The researchers suggested that more interest should be paid to the design of the strut to minimize the pressure loss while maintaining the ability to affect the flow field.

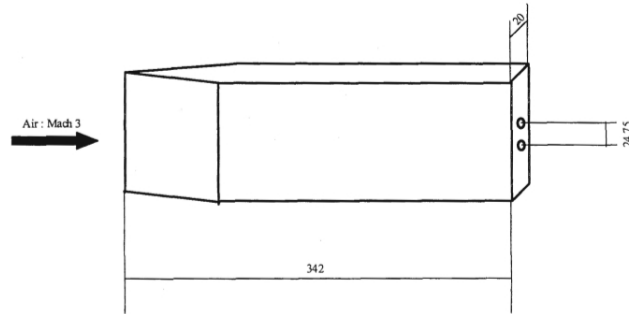


Figure 2.6: Strut used in Ref [12]

Many researchers [13–15] looked at modifying the trailing edge of the vertical strut to increase mixing. The basic strut design was similar in that the strut was connected to the top and bottom of the test section and the leading edge was a wedge. The difference came from the trailing edge designs as seen in Figure 2.7. The different trailing edges, called alternating wedge designs, create either co-rotating or

counter-rotating vortices that are used to enhance the mixing. All of these designs use parallel fuel injection at the trailing edge of the strut so that the fuel is entrained into the vortices which cause the increased mixing in the combustion section. The results from this research concluded that the alternating wedge design created a more uniform mixing region, but the overall combustion performance is similar to that of a strut with a flat trailing edge and causes a larger total pressure loss.

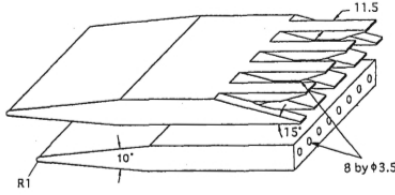


Figure 2.7: Alternating Wedge strut used in Ref [13]

NASA conducted research at the Lewis Research center [16] on struts and studied the effects of the geometric parameters of the strut on the drag in the combustion section. The drag that develops in the combustion section must be balanced by the thrust produced by the engine. Therefore, the drag should be low for more efficient scramjet designs. The struts used in this experiment [16] had a diamond shaped cross section, Figure 2.8, instead of the wedge leading edge and box shaped body. Unlike the struts used in previous research, these struts did not connect to the top and bottom of the test section. These struts used normal injection at the thickest part of the strut. NASA compared nine different struts with variations in the position of maximum thickness, thickness, leading edge sweep and length. The largest contributor to the drag was the thickness of the strut, a slight decrease in the thickness lead to a 50% reduction in the drag. Also, increasing the leading edge sweep decreased the drag of the strut.

Research conducted by the Air Force Research Lab [4] examined three different strut shapes and their effect on the combustion in a Scramjet chamber. These struts are similar to the NASA struts in that they are not connected to the bottom and top of the test chamber and have a leading edge sweep angle, but did not have the

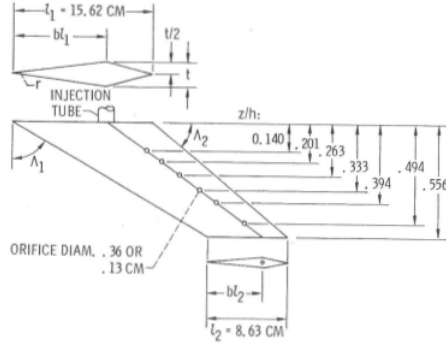


Figure 2.8: Diagram of basic strut from Ref [16]

diamond body of the NASA struts, as in Figure 2.9. Unlike previous research, these struts are placed directly in front of the combustion cavity used for holding the flame of the combustion. The three struts tested had slightly different trailing edges, a flat trailing edge, a 45 degree trailing edge similar to a tapered airfoil, and the third had an extension that went into the combustion cavity. Testing was done in a supersonic research facility using a continuous air flow at a Mach number of 2. Their research showed an increase in maximum temperature and mixing, as well as moving the center of combustion into the main section of the flow as compared to a cavity without a strut. As in previous research, the strut included fuel injection into the flow, but here the fuel was injected from the leading edge of the strut.

2.4 Current Research

The results of the AFRL/RZ research, combined with the NASA geometric evaluation, generated interest in evaluating the effects of the strut geometry on the mixing and combustion. The three struts from the AFRL research will be used as a baseline and the results from the AFRL research will be used to configure the computational solver. Variations in the height and width of the three baseline struts will be tested by computational analysis. The results from these tests will compare the total pressure loss and the combustion area as measurements of the overall combustion performance. These results can be used to design more efficient struts for use in

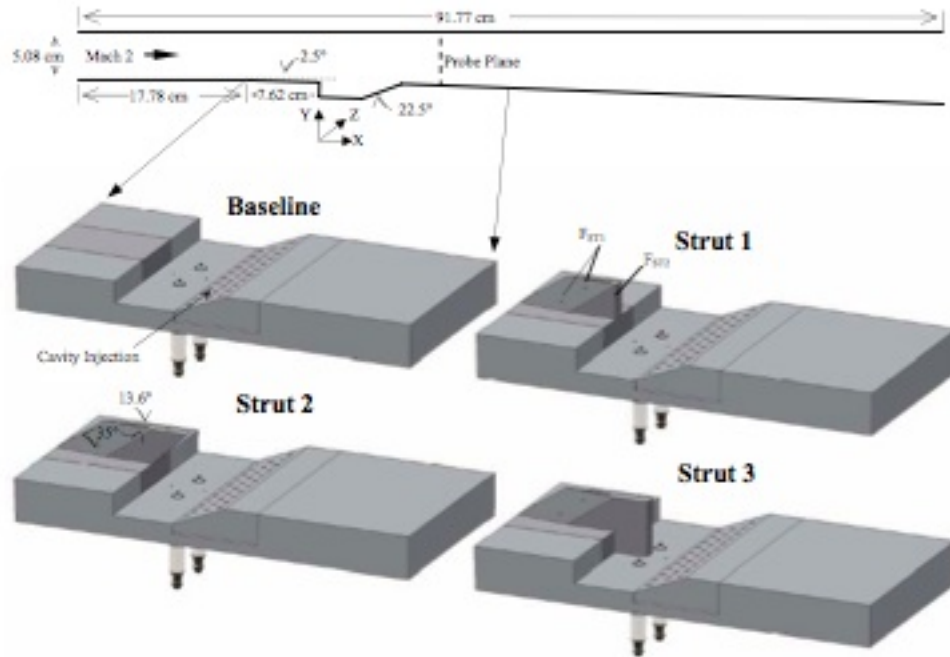


Figure 2.9: Image of struts used in AFRL research [4]

scramjet combustion sections. A better strut design could lead to shorter combustion sections and therefore shorter scramjet engines for real world use.

III. Computational Setup

3.1 Computational Domain

The computational domain used in this study is the same as the supersonic research facility (Research Cell 19) as used in the previous research [4], located at the Air Force Research Laboratory, Propulsion Directorate. The inlet into the domain is 5.08 cm tall and 15.24 cm wide rectangular duct. The duct continues at a constant area for 17.78 cm, at which point the floor takes a 2.5 degree turn down. The floor continues for 7.62 cm where the strut is placed. The combustion cavity is placed directly behind the strut. The cavity is 1.65 cm deep and 4.57 cm long and is shown in Figure 3.1. The back wall of the cavity is slanted at 22.5 degrees and has two rows of injectors, the bottom row for fuel and the top row for air. All injection ports in the cavity and on the strut have a diameter of 0.16 cm. The computational domain ends in a diffuser making the total length of the domain 91.77 cm. Figure 3.2 shows the view of the domain from the side with the baseline strut installed. The cartesian coordinate system of the domain are as follows; the positive x-direction is along the main flow direction from the inlet to the outlet, positive y-direction is from the floor to ceiling, and the positive z-direction goes from left wall to the right when viewed from the inlet.

3.1.1 Struts. The struts are placed just before the cavity with the leading edge at the point where the bottom floor turns 2.5 degrees. For this research, 15 strut designs were compared. Three of these designs are those used in an AFRL research project [4] and are used as baseline struts to compare with the 12 other designs. The side view of the three baseline struts are shown in Figure 3.3. Strut 1, referred to as S1B, is 7.62 cm long, 2.54 cm tall, and 0.95 cm wide. The leading edge sweep angle is 35 degrees and the wedge angle is 13.6 degrees. The struts also have three fuel injectors, each spaced 0.635 cm vertically but angled at 35 degrees to be parallel to the leading edge of the strut. When viewed from the inlet, two of these injectors are on the right side of the strut and the middle injector is on the left. Strut 2, S2B, adds a 2.54 cm extension to the top of trailing edge of S1B, while the base length

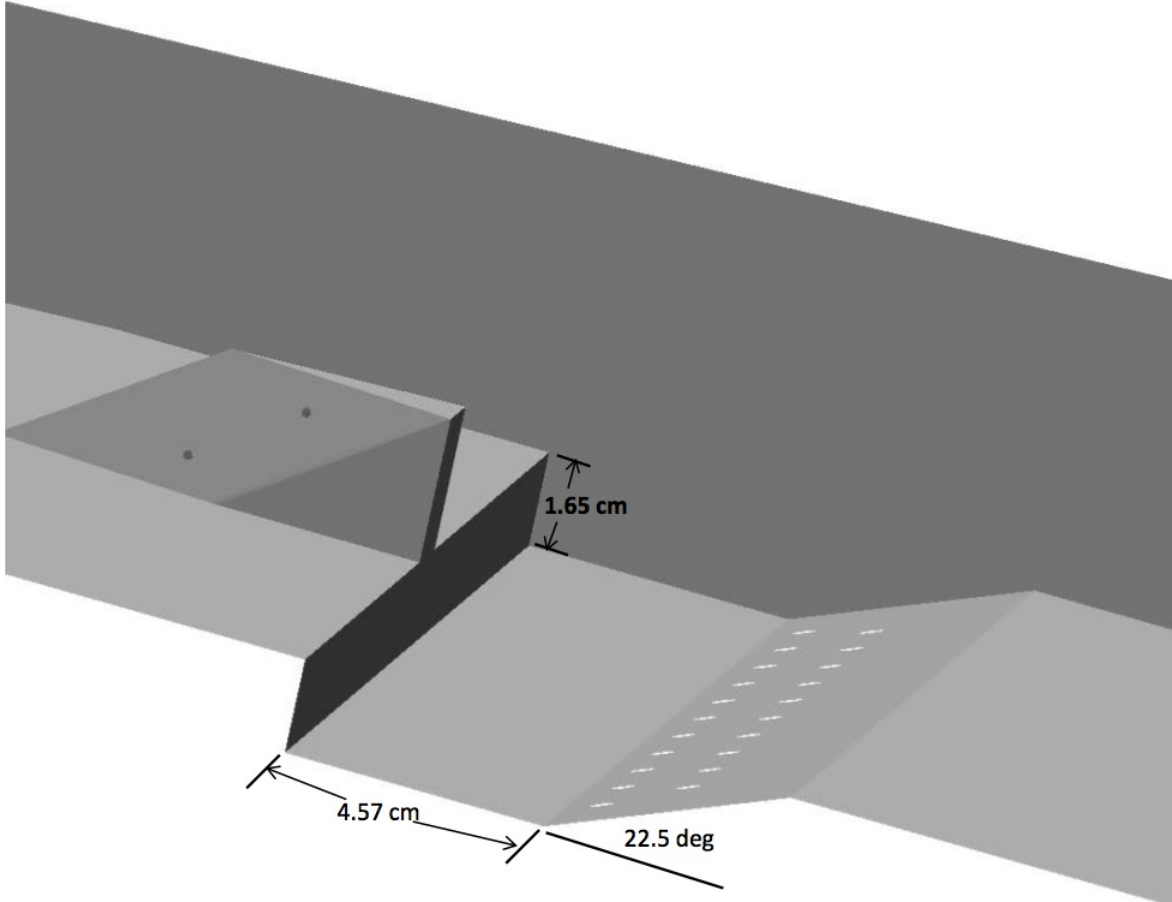


Figure 3.1: Side view of computational domain

remains the same. The extension creates a 45 degree angle on the trailing edge over the cavity. The third strut, S3B, uses the same 2.54 cm extension but the extension continued down to the floor of the cavity.

The 12 other strut designs that were derived from these baseline struts had their height and width increased and decreased by 50% of the baseline value. All other parameters of the baseline struts are the same. Throughout the paper the struts will be referred by the name of the baseline strut and size variation; the short strut will be referred to as strut H1, the tall strut is H2, the thin strut is W1 and the wide strut is W2. As an example, the tall version of Strut 2 is S2H2. Figure 3.4, 3.5 and 3.6 show a relative comparison between the different heights and widths.

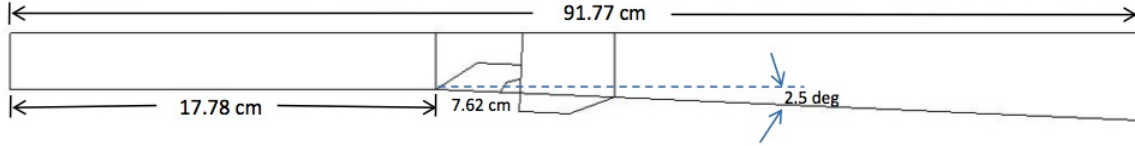


Figure 3.2: Dimensions of the cavity

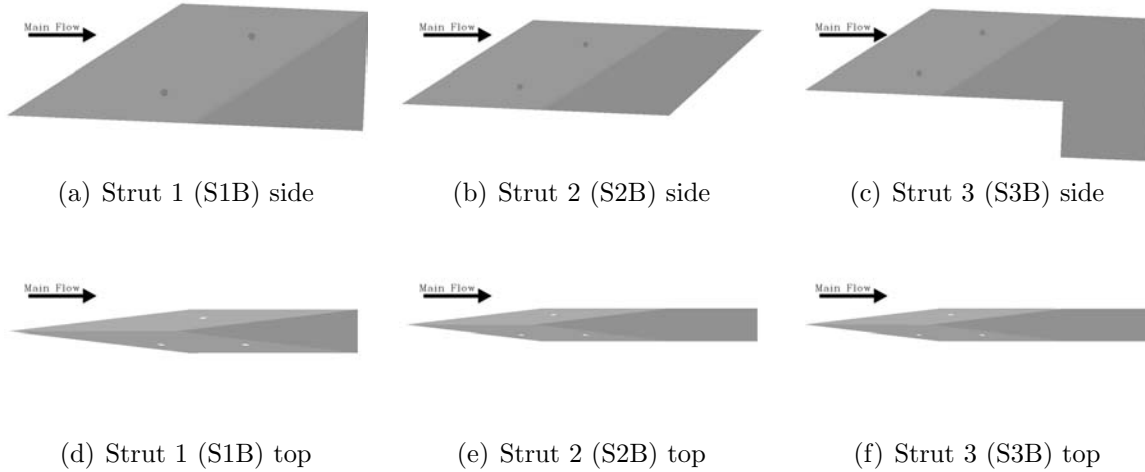


Figure 3.3: The three baseline struts

3.1.2 Inflow Conditions. In the computational domain there are four boundary conditions where flow enters the domain: the main inlet, the strut injectors, the cavity air injectors, and cavity fuel injectors. Of these four inflow conditions, two inject air and two inject fuel into the computational domain. The two air inflow conditions are the main inlet to the computational domain and the top row of injectors in the cavity. The air inflow conditions model air as a mixture of 23.14% O_2 and 76.86% N_2 by mass. Flow in the main inlet is at a Mach number of 2 or 725.8 m/s in the positive x-direction. The other fluid properties of the main inlet are a static temperature of 327.77 K and a static density of 0.2826 kg/m^3 . The main inlet includes 1% turbulence in the flow to model the turbulence created by the wind tunnel prior to the computational main inlet. Since the wind tunnel this computational domain was based on starts before the main inlet of the computational domain, there would be a boundary layer formed at the main inlet. The incoming boundary layer was not

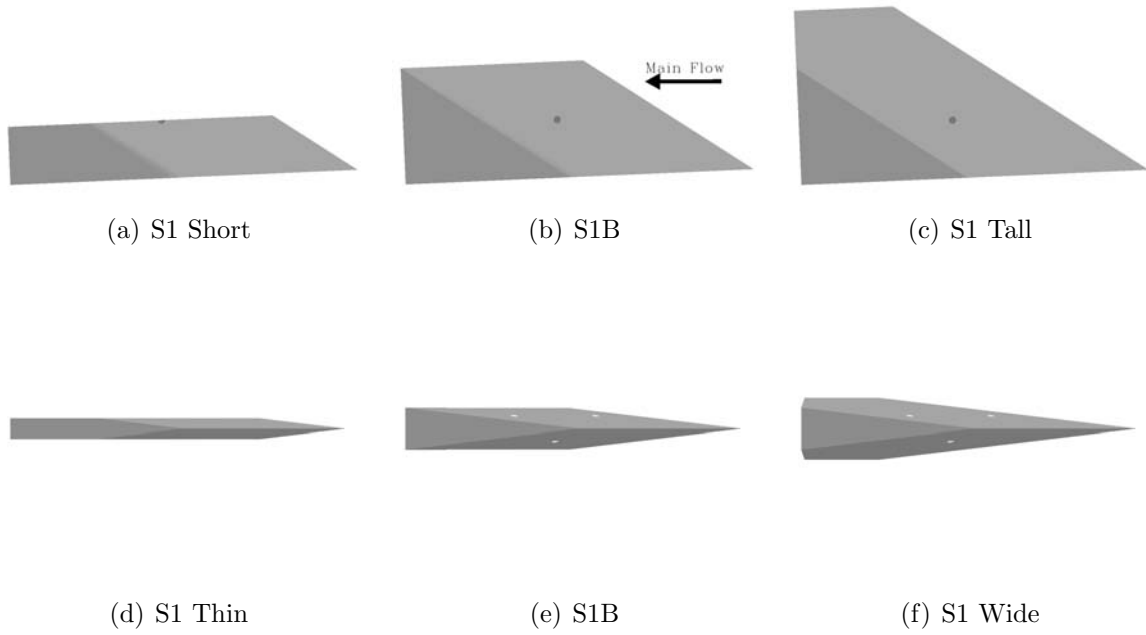


Figure 3.4: Comparison of different strut 1 sizes

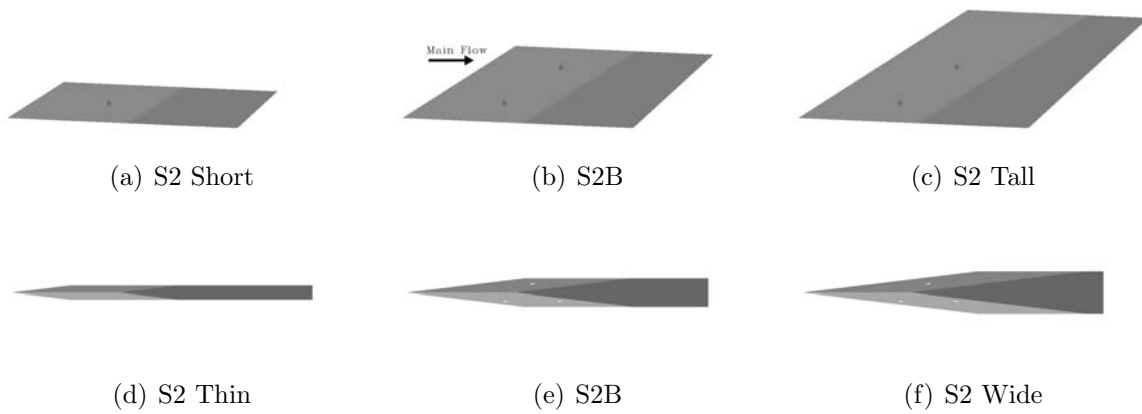


Figure 3.5: Comparison of different strut 2 sizes

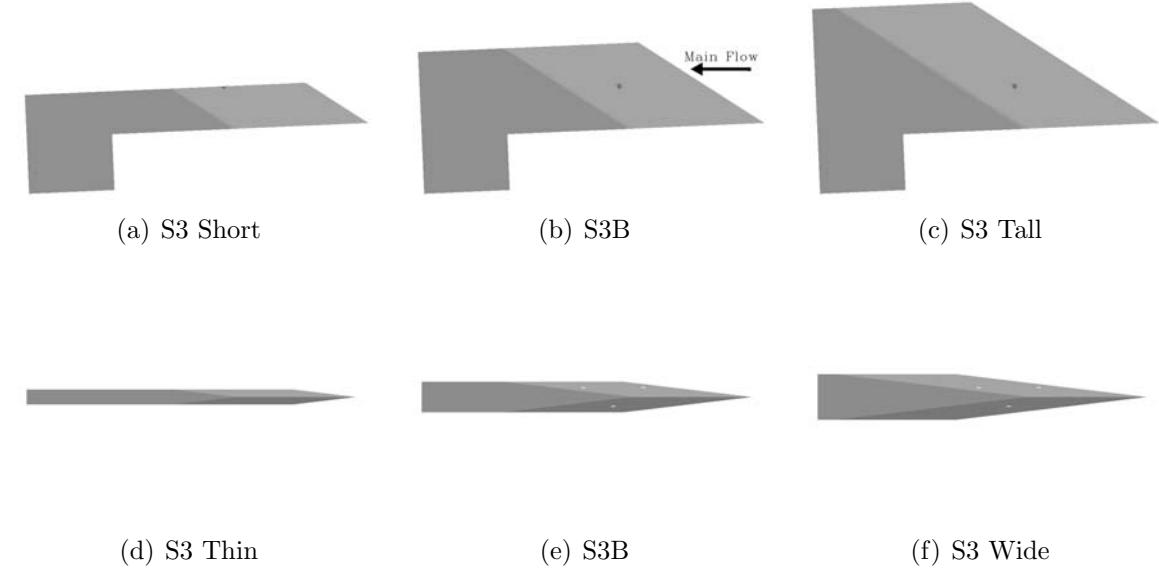


Figure 3.6: Size comparison for strut 3

modeled because no data exists on the shape of the boundary layer. The entire wind tunnel was not modeled to reduce the time required for grid generation and computational run time. The 10 cavity air injectors inject air opposite to the main air flow, or negative x-direction (Figure 3.7), at a velocity of 384.7 m/s. Due to this lower velocity, the static temperature is 504.843 K and a static density of 0.8115 kg/m³.

The two fuel injection flow conditions are found on the strut and in the lower row of 11 injectors in the cavity as shown in Figure 3.7. Both inflow conditions inject ethylene (C₂H₄) as the fuel into the computational domain. The three strut inflow boundaries inject ethylene at 205.06 m/s in the positive and negative z-direction depending on which injector on the strut is considered. The ethylene injected has a static temperature of 542.35 K and static density of 0.9544 kg/m³. The 11 injectors in the cavity inject the fuel in the negative x-direction at a velocity of 70.2 m/s. At this low velocity, the static temperature is 573.23 K and the static density is 1.096 kg/m³.

All of these flow conditions are set by matching the setup from the original AFRL/RZ experiment [4]. The reference conditions used in the VULCAN computational fluid dynamics (CFD) package are a total pressure of 410 kPa and total

Table 3.1: Inlet Conditions

Inflow	Velocity (m/s)	Density (kg/m ³)	Composition (by mass)
Inlet	725.8	0.2826	23.14% O ₂ 76.86% N ₂
Cavity Air	384.7	0.8115	23.14% O ₂ 76.86% N ₂
Strut Injectors	205.06	0.9544	100% C ₂ H ₄
Cavity Fuel	70.2	1.096	100% C ₂ H ₄

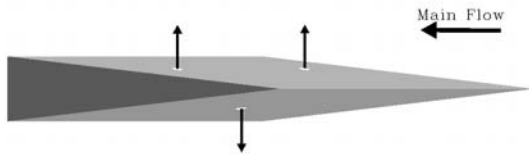
temperature of 590 K, which are the total pressure and temperature of the main inlet flow.

3.2 *VULCAN Code*

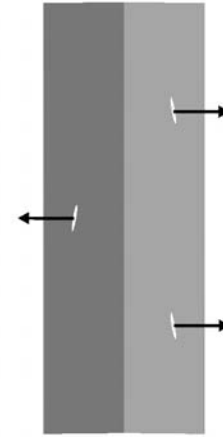
The Viscous Upwind Algorithm for Complex Flow Analysis [17] (VULCAN) from NASA’s Hypersonic Air Breathing Propulsion Branch was used for this research. VULCAN is used for turbulent reacting and non-reacting flow at speeds from subsonic to hypersonic. The code uses several different convergence acceleration techniques to reduce time required for test cases. All 15 struts were evaluated as steady turbulent viscous flow without reactions. The $k-\omega$ turbulence model was used. The flux scheme used was the blended low dissipation flux split scheme/van Leer scheme (LDFSSB) with a second order Fromme MUSCL scheme with a smooth limiter [17].

3.2.1 Laminar and Turbulent. At the beginning of this research, five laminar cases were run. These laminar cases only evaluated the five struts based on S1B. Laminar results are not expected to give accurate results, but are used to highlight trends. While only the five cases were run to convergence, all 15 struts had at least 4000 laminar iterations run before using turbulence to avoid instabilities that occurred when initially running turbulent cases.

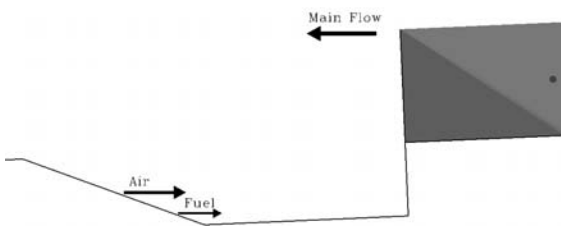
The $k-\omega$ turbulence model was used because it balances accuracy and computational requirements. The $k-\omega$ is a two equation turbulence model. VULCAN only includes eight turbulence models, three of which are not useable for the flow condition in these simulations. There were still two more complex turbulent models that could be used, both variations of the Menter turbulence model. A comparison test was run



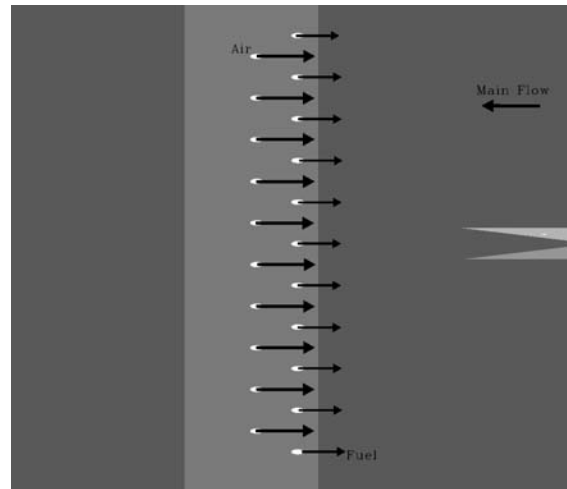
(a) Strut injectors top



(b) Strut injectors front



(c) Cavity side



(d) Cavity top

Figure 3.7: Location and direction of injectors

very early in this research and it was found that the $k-\omega$ model required less time per iteration. Since time is a factor in this research, the $k-\omega$ model was selected.

3.2.2 Non-reacting flow. Initially, the inclusion of reactions in these simulations was used. The reaction equations modeled the combustion of ethylene in air. The reaction were removed to reduce the time required for each iteration. Removing the reaction equations reduced the clock time for each iteration by 12 seconds. Since reactions were used at the beginning of these simulations, some residual species maybe present.

3.2.3 Steady Flow. All 15 cases were run in a steady state mode. A steady state solution assumes the solution is not dependent on time. In these simulations there are expected to be unsteady vortex generation caused by the strut. Steady state solutions were used in these simulation because an unsteady solution would require more time and computational resources. While unsteady simulations would give an accurate depiction of the vortex generation, the steady state solutions would supply the effects of height and width of the strut on the performance parameters. Running steady state solutions also affect the reduction of the residuals used to measure convergence since the unsteady flow structures cause the residuals to fluctuate.

3.2.4 Flux Scheme. For these simulations, a blended low dissipation/van Leer flux splitting scheme was used. The van Leer flux splitting scheme decomposes the vector of conserved variables based on the characteristics of the convective fluxes. This scheme functions at all speed regimes for the Euler flow equations. When the van Leer scheme is applied to the Navier-Stokes equations, it has difficulties resolving the boundary layer [18]. The boundary layer is where the low dissipation flux splitting scheme (LDFSS) is applied. LDFSS assists in resolving the boundary layer and the discontinuities created by shocks by merging flux splitting with flux differencing. Flux differencing not only tracks the characteristics of the flow, but also the characteristics themselves. Incorporating the characteristics allows for better resolutions of shocks

and other discontinuities. The LDFSSB scheme blends van Leer and LDFSS to take advantage of the strengths and balance the weaknesses of each flux scheme.

3.2.5 Convergence Criteria. In these simulations, the flow is inherently unsteady and vortex shedding is expected behind the struts. Due to this unsteady vortex shedding, the reduction of the residuals in the VULCAN code cannot be the only measure of convergence. The mass flow rate error, \dot{M}_{error} , is used as the first of the convergence criteria. The mass flow rate error is the error between the flow from all of the inflow boundary conditions, \dot{M}_{in} , and the mass exiting the outlet, \dot{M}_{out} :

$$\dot{M}_{Error} = \frac{\dot{M}_{in} - \dot{M}_{out}}{\dot{M}_{in}} \quad (3.1)$$

When the mass flow rate error is less than 1%, this criteria is assumed satisfied. The second measure of convergence is the reduction of the residuals by two orders of magnitude. For the five laminar cases, this occurred at about 10,000 iterations and took about 72 clock seconds per iteration. The turbulent cases on average required 40,000 iterations on top of any laminar iterations before reaching convergence. The turbulent iterations required about 100 clock seconds per iteration. Part of the increase in clock time is due to the 15 turbulent cases being processed on two processors instead of the four processors used for laminar.

3.3 Grid Generation

The grids built for these tests ranged from 3.8 to 4.5 million cells depending on which strut was modeled, most of which were concentrated near the strut and in the combustion cavity. To capture the boundary layer of the flow along the walls of the test section and on the strut, the parameter Y^+ is used. Y^+ is a non-dimensional wall distance used to estimate a location in the boundary layer and calculated by:

$$Y^+ = \frac{u_* y}{\nu} \quad (3.2)$$

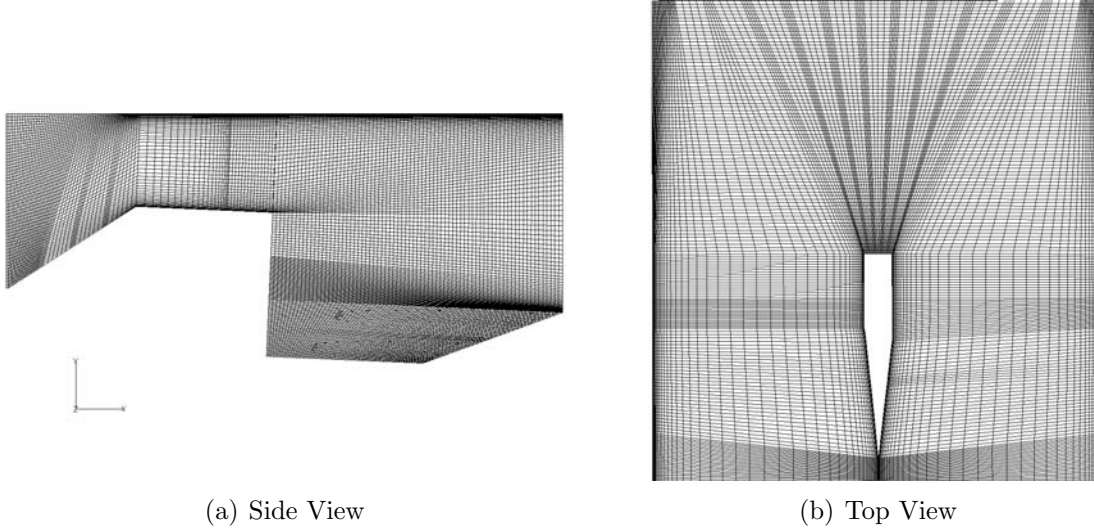


Figure 3.8: Views of grid

In the previous equation, u_* is the friction velocity, y is the distance to the wall and ν is the kinematic viscosity. The friction velocity used was 4.4 m/s based on estimated wall shear stress and the kinematic viscosity of air was used. The VULCAN CFD solver uses wall functions for near wall calculations and requires the grid to have a minimum Y^+ value of 20. The Y^+ value translated to a value of 0.0127 cm spacing at the wall for all cases. The grid was then spaced using a geometric scheme with a growth factor of 1.2. The Y^+ was enforced on all walls of the domain and on the strut. The grid density on the walls of the strut created increased grid density behind the strut. Figure 3.8 shows the side and top view of the grid around the strut and combustion cavity. A grid convergence study was not accomplished for these grids due to their size, and experts advised that the grids were already denser than was required.

All of the 15 grids used a structured grid layout. A structured grid requires all cells in the grid to be six-sided, preferably cubic in shape. Unfortunately, the shape of the struts required extensive grid generation in order to maintain the six-sided nature of a structured grid. For the surface grids, a structured grid appears as four-sided cells. The combination of the wedge leading edge and the width of the strut creates a triangle shaped zone as seen in Figure 3.9. To create four-sided domains to create

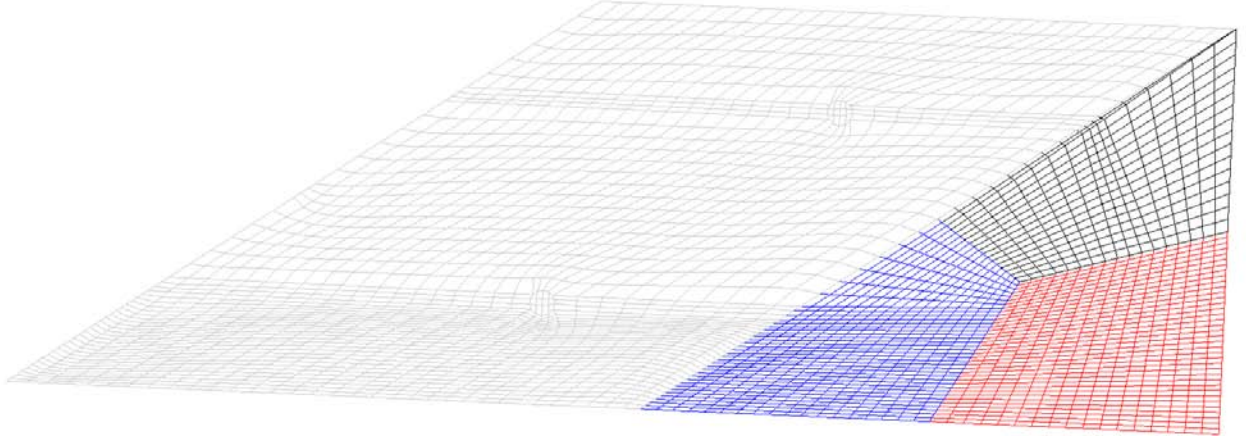


Figure 3.9: View of domains on side of Strut S1B

a structured grid, the midpoints of the three lines were marked and used to create three connectors to make the proper four-sided domains. Another part of the strut that required extensive grid generation were the injection ports, Figure 3.10. Since the injectors are circular, they were split into four connectors. To make the injectors work on the strut, connectors were used to connect the leading edge to the injector and from the injector to the edge of the triangular area mentioned earlier.

The top of the strut was another triangular area that required modification to maintain a structured grid. The top of the strut was split into two domains by placing connectors angled opposite the triangle. The new connectors create a skewed rectangular shape that can be used to generate the structured domain. The two domains allow the top of the strut to maintain the four-sided cells as shown in Figure 3.11.

The last area that required unusual grid generation was the back face of the cavity where the injection ports are found. As with the injectors on the struts, the injectors in the cavity had to be split into four connectors. To make the injectors work within the domain of the cavity back wall, slanted connectors were used to make four-sided domains. The purpose of the slanted connectors was to avoid skewness issues that occurred without the connectors. Figure 3.12 shows the final domain

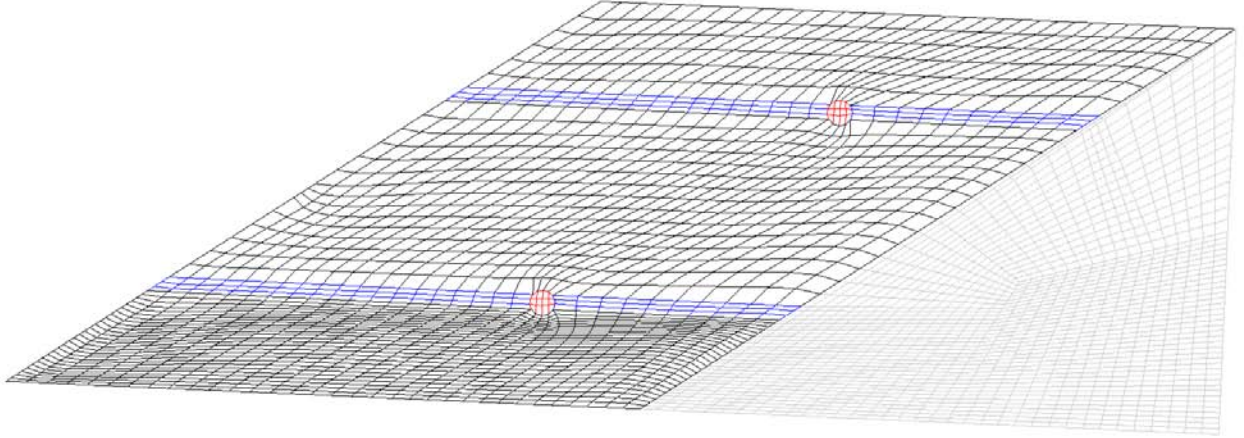


Figure 3.10: Injector domains on side of Strut S1B

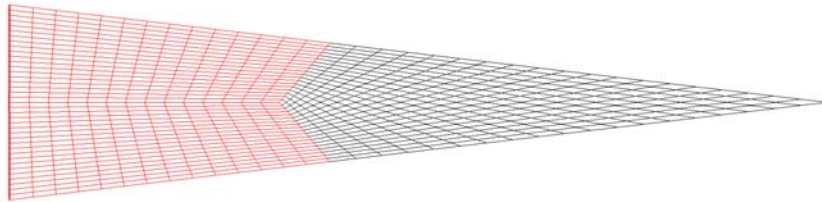


Figure 3.11: Top view of domains on Strut S1B

configuration for the back face of the cavity. In Figure 3.12, the injector appears elliptical due to the slant of the back face of the cavity and the circular injector port.

3.4 Data Collection

The CFD results are post-processed in FieldView[®]. VULCAN outputs grid and function files formatted for FieldView[®]. The function files contain the values of selected parameters at each cell in the grid. FieldView[®] was used over Tecplot[®] since the large size of the grid cause malfunctions while attempting to load the data. The two key parameters to be measured are the total pressure loss and the equivalency ratio.

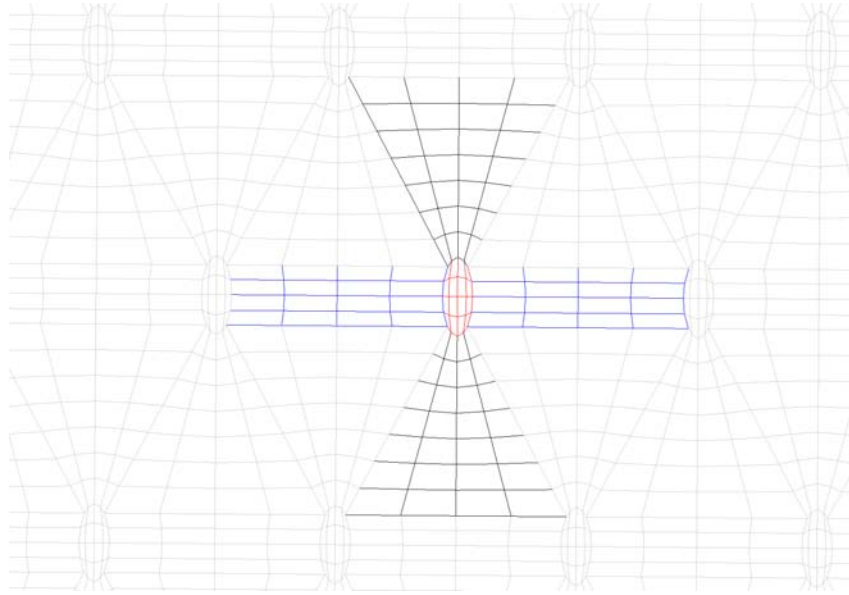


Figure 3.12: Domain configuration in the cavity

Three planes were used to collect total pressure, velocity profiles and equivalence ratio measurements. The first location is near the midpoint of the combustion cavity, the third is at the exit of the cavity and the second measurement location is halfway between the others. The locations are labeled by the distance from the inlet to the plane, and all calculation do not include the combustion cavity since it is not the focus of this research. The three data measurement planes are shown in Figure 3.13

3.4.1 Total Pressure Loss. The total pressure loss of the scramjet engine is a key measure of the efficiency of the engine. To find the total pressure loss across the combustion section, a measurement is taken just before the strut and at the exit of the cavity. The first measurement was taken at the point when the floor of the computational domain takes a 2.5 degree bend. The second measurement is after the back edge of the cavity. The planes are constant x planes and cover the whole range of y and z directions. To find the pressure, the integration function of FieldView[®] is used. The integration function outputs the area averaged total pressure, P , across the plane. The area averaged total pressure was used over mass averaged pressure since the flow is not expected to have large density gradients. Using the average of

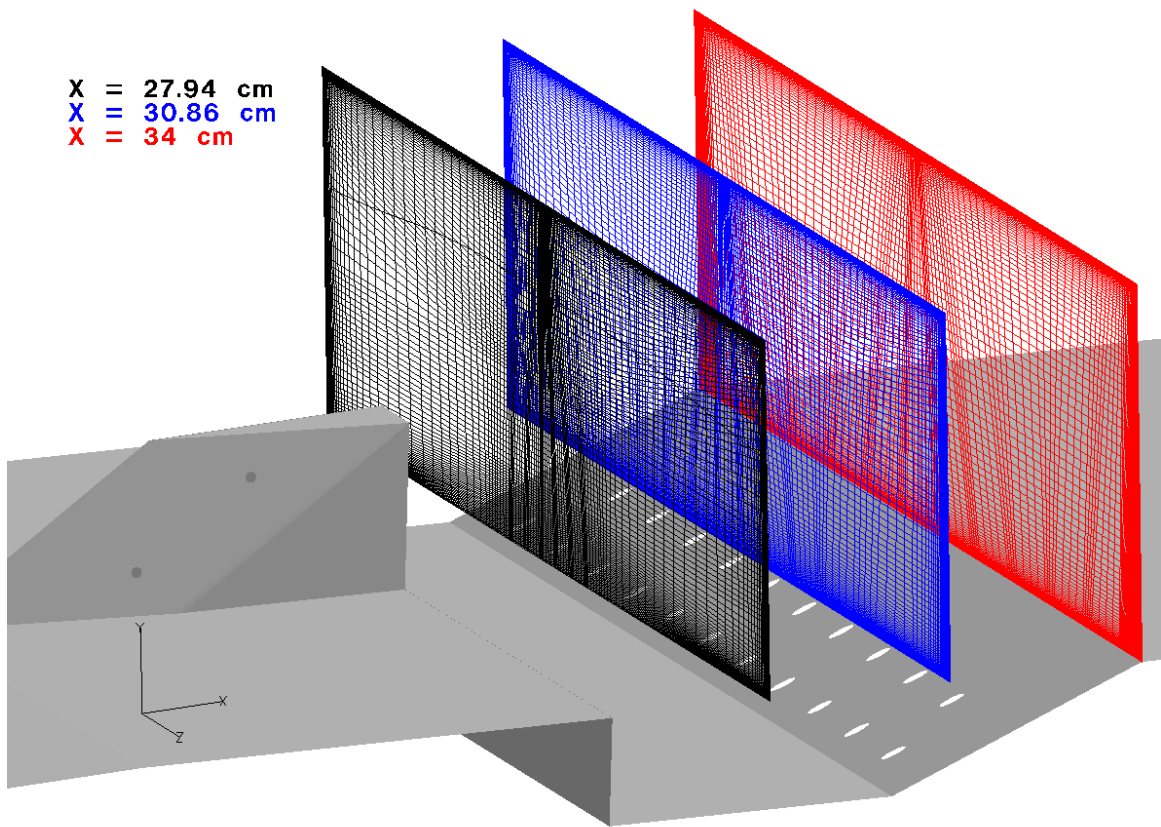


Figure 3.13: Planes used for data collection

the total pressure at both planes, the total pressure loss ratio is found by:

$$P_{loss} = \frac{P_{out}}{P_{in}} \quad (3.3)$$

Where P_{loss} is the total pressure loss ratio, P_{in} is the average pressure at the first plane before the combustion section and P_{out} is the average pressure at the exit of the combustion section.

3.4.2 Equivalence Ratio. The equivalence ratio (Φ) compares the mixing of the fuel and air to the stoichiometric fuel to air ratio ideal for combustion. An equivalence ratio of 1 means the flow is mixed at stoichiometric conditions. The value of the equivalence ratio shows where the flow is capable of combustion. The equivalence ratio is calculated by Equation 3.4.

$$\Phi = \frac{m_{fuel}/m_{air}}{(m_{fuel}/m_{air})_{st}} \quad (3.4)$$

In Equation 3.4, m_{fuel} is the mass of the fuel, m_{air} is the mass of the air, and the subscript st defines the stoichiometric conditions. VULCAN does not output mass, but mass fractions, Y , as:

$$Y_{N_2} = \frac{m_{N_2}}{m_{total}} \quad (3.5)$$

$$Y_{O_2} = \frac{m_{O_2}}{m_{total}} \quad (3.6)$$

$$Y_{fuel} = \frac{m_{fuel}}{m_{total}} \quad (3.7)$$

In the above equations, m_{N_2} is the mass of nitrogen, m_{O_2} is the mass of oxygen, and m_{total} is the total mass of the mixture. The mass fractions above can be used to rearrange the equivalence ratio along with the mass fraction for air, Y_{air} . VULCAN does not output Y_{air} , so the numerator of Y_{air} multiplied by m_{N_2}/m_{N_2} ,

$$Y_{air} = \frac{m_{air}}{m_{total}} = \frac{\frac{m_{N_2}}{m_{N_2}} m_{air}}{m_{total}} = \frac{m_{N_2}}{m_{total}} \frac{m_{N_2}}{m_{air}} \quad (3.8)$$

Y_{air} is equal to $Y_{O_2} + Y_{N_2}$ but this derivation will be dependent only on Y_{N_2} and the inlet conditions. Since N_2 is a component of air and inlet flow is only air,

$$\frac{m_{N_2}}{m_{air}} = \text{constant} = \left(\frac{m_{N_2}}{m_{total}} \right)_{inlet} = (Y_{N_2})_{inlet} = 0.7686 \quad (3.9)$$

Substituting the previous equation back into Equation 3.8

$$Y_{air} = \frac{Y_{N_2}}{(Y_{N_2})_{inlet}} \quad (3.10)$$

Assuming the mixture is of fuel and air, and nitrogen and oxygen are only injected as air,

$$Y_{fuel} = \frac{m_{fuel}}{m_{total}} = 1 - Y_{air} \quad (3.11)$$

Returning to Equation 3.4, both m_{air} are multiplied by m_{O_2}/m_{air}

$$\Phi = \frac{m_{fuel}/m_{air}}{(m_{fuel}/m_{air})_{st}} = \frac{m_{fuel}/\frac{m_{O_2}}{m_{air}}m_{air}}{\left(m_{fuel}/\frac{m_{O_2}}{m_{air}}m_{air} \right)_{st}} = \frac{m_{fuel}}{m_{O_2}} / \left(\frac{m_{fuel}}{m_{O_2}} \right)_{st} \quad (3.12)$$

The both components of the numerator is then multiplied by $1/m_{total}$

$$\Phi = \frac{\frac{m_{fuel}}{m_{total}}}{\frac{m_{O_2}}{m_{total}}} / \left(\frac{m_{fuel}}{m_{O_2}} \right)_{st} \quad (3.13)$$

In the previous equation, m_{fuel}/m_{total} can be replaced by Y_{fuel} . In m_{O_2}/m_{total} , m_{O_2} is replaced by,

$$m_{O_2} = m_{air} \left(\frac{m_{O_2}}{m_{total}} \right)_{inlet} \quad (3.14)$$

Since $m_{total,inlet} = m_{air}$. Therefore the equivalence ratio becomes:

$$\Phi = \frac{Y_{fuel}}{\frac{m_{air}}{m_{total}} \left(\frac{m_{O_2}}{m_{total}} \right)_{inlet}} / \left(\frac{m_{fuel}}{m_{O_2}} \right)_{st} = \frac{Y_{fuel}}{Y_{air}(Y_{O_2})_{inlet}} / \left(\frac{m_{fuel}}{m_{O_2}} \right)_{st} \quad (3.15)$$

Using Equations 3.10, 3.11 and 3.15, the value for the equivalence ratio can be found by using the inlet conditions, the constant stoichiometric fuel to air ratio,

$(m_{fuel}/m_{O_2})_{st} = 0.2922$, and the mass fraction of N_2 . The mass fraction of N_2 was collected as an output from the VULCAN solver.

The equivalence ratio was calculated at three planes in the combustion section as seen in Figure 3.13. It is assumed that combustion can occur at an equivalence ratio of 0.2 to 2 [19]. Using this as a limit, the combustion area at each of the planes is calculated.

IV. Results and Discussion

Laminar simulations were completed for S1B, S1H1, S1H2, S1W1, and S1W2 before the turbulent cases. In the laminar simulations the results for the total pressure loss and equivalence ratio are presented. Due to the unsteady nature of the flow field, the laminar results are expected to show lower pressure losses and lower combustible area than the later turbulent cases due to the lack of turbulent mixing.

The transition from laminar to turbulent simulations can be difficult. Even with precautions, as in reducing the CFL number, the turbulent simulations contained cells that had to be limited by the minimum and maximum temperature limits of the VULCAN solver. The CFL number is the ratio of the physical speed to the computational speed. By reducing the CFL number, the solver uses smaller spatial steps during an iteration. The reduction of the spatial step increases the stability of the solver but at a cost of more iterations to reach the same solution. The limited cells were primarily located in the boundary layer and could be a source of error in the simulations. To remove the limited cells, more iterations are required than was possible with the time required for this research. The limited cells were not as large an issue for S1 struts due to the 10,000 iterations at laminar conditions used as a base for the turbulent simulations. The reduction of the CFL number caused an increase in the required number of iterations for turbulent results. Due to the increase in required iterations, S2B and S3B and their variants did not reach full convergence in the time allowed for these simulations. While the lack of full convergences may not give accurate results, they did allow for capturing the trends caused by the geometric changes.

4.1 *Total Pressure Loss*

The loss of total pressure is mostly caused by the size of the strut in the flow through the combustion section. The strut creates a pocket of low pressure and low speed air in its wake that allows for mixing and the creation of a flame zone. Figure 4.1 and Figure 4.2 show velocity vectors behind the strut from the side and top views

respectively. The strut creates a recirculation region behind it, allowing for fuel and air to mix. In Figure 4.1, the flow travels from the cavity up the back face of the strut, and into the main flow. It is expected that the larger struts create a larger recirculation region, and thus suffer greater total pressure losses.

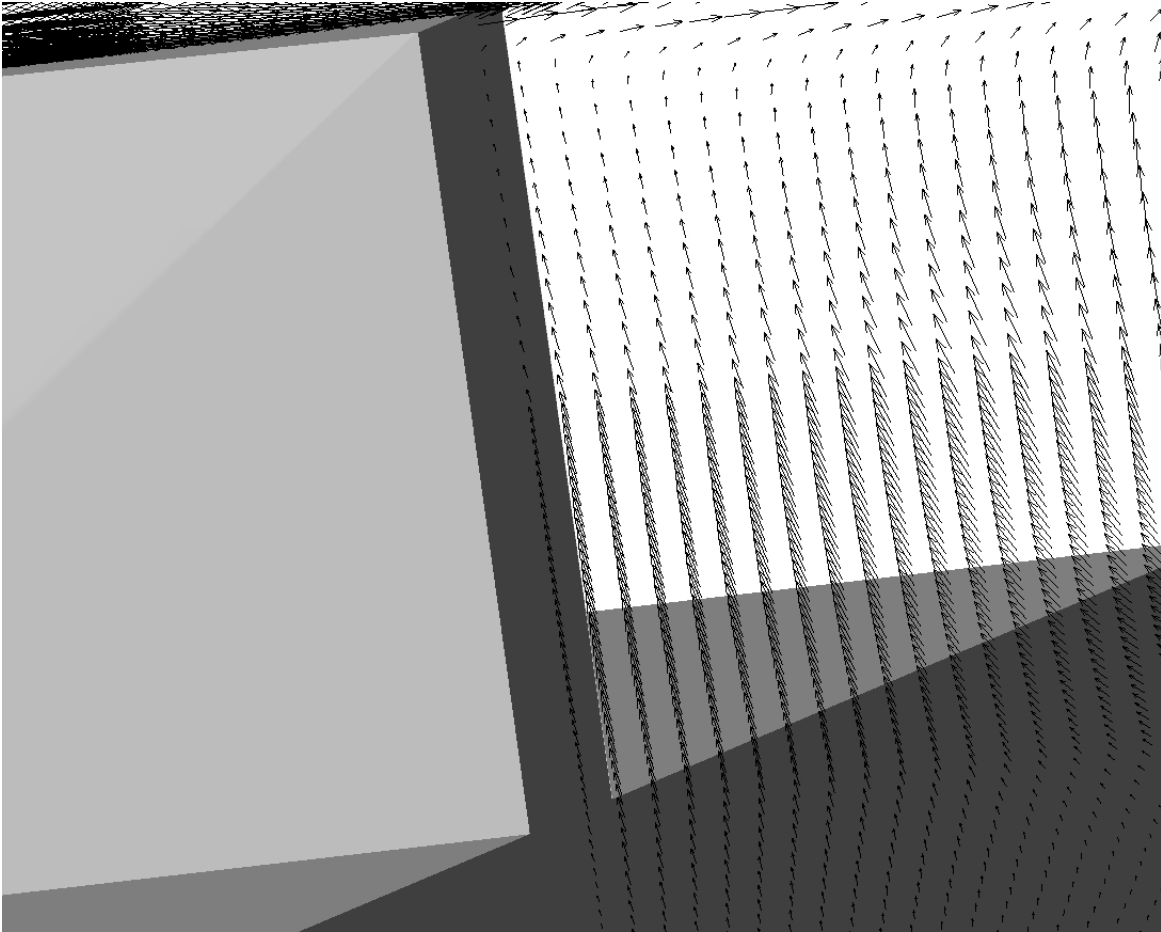


Figure 4.1: Side view of velocity vectors behind strut

4.1.1 Laminar. The pressure ratio was calculated and compiled in Table 4.1. The struts with the largest cross sectional area, S1H2 and S1W2, have the most pressure loss across the combustion section. These results were expected since the larger cross section would cause a larger pressure loss due to the low pressure region behind the strut. The low pressure wake behind the strut entrains the fuel-air mixture from the cavity into the main flow of the combustion section. The two struts with

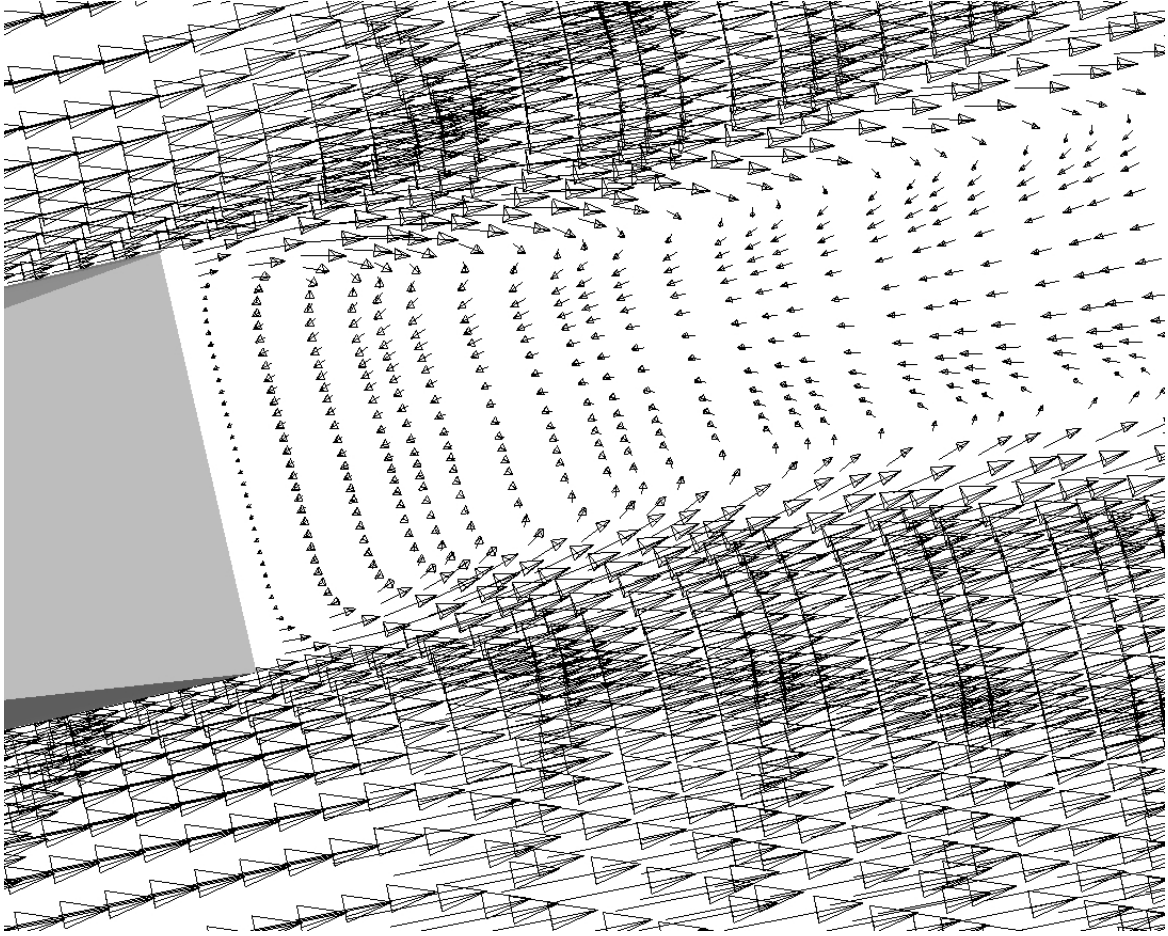


Figure 4.2: Top view of velocity vectors behind strut

smaller cross sections, S1H1 and S1W1, have the least pressure loss, due to the smaller cross sectional area. Figure 4.3 shows the total pressure contours at the exit of the combustion section. The low pressure region in the center of each images is relative in size to the total pressure loss of each strut.

4.1.2 Turbulent Results. The total pressure loss for S1B and the four variants follow the same trends as the laminar results. Strut S1H2 and S1W2 have the largest pressure loss due to the increased blockage of the flow. Strut S1H1 and S1W1 have a lower pressure loss. The total pressure loss ratios are shown in Table 4.2 along with the total pressure at the two measurement planes between the entrance and exit of the combustion section. The table shows that the total pressure drops throughout

Table 4.1: Laminar total pressure ratio across combustion section

Strut	P_{in} (Pa)	P_{out} (Pa)	$\frac{P_{out}}{P_{in}}$
S1B	586503	527487	0.899
S1H1	586039	535985	0.915
S1H2	587950	518819	0.882
S1W1	588724	534007	0.907
S1W2	586678	516568	0.880

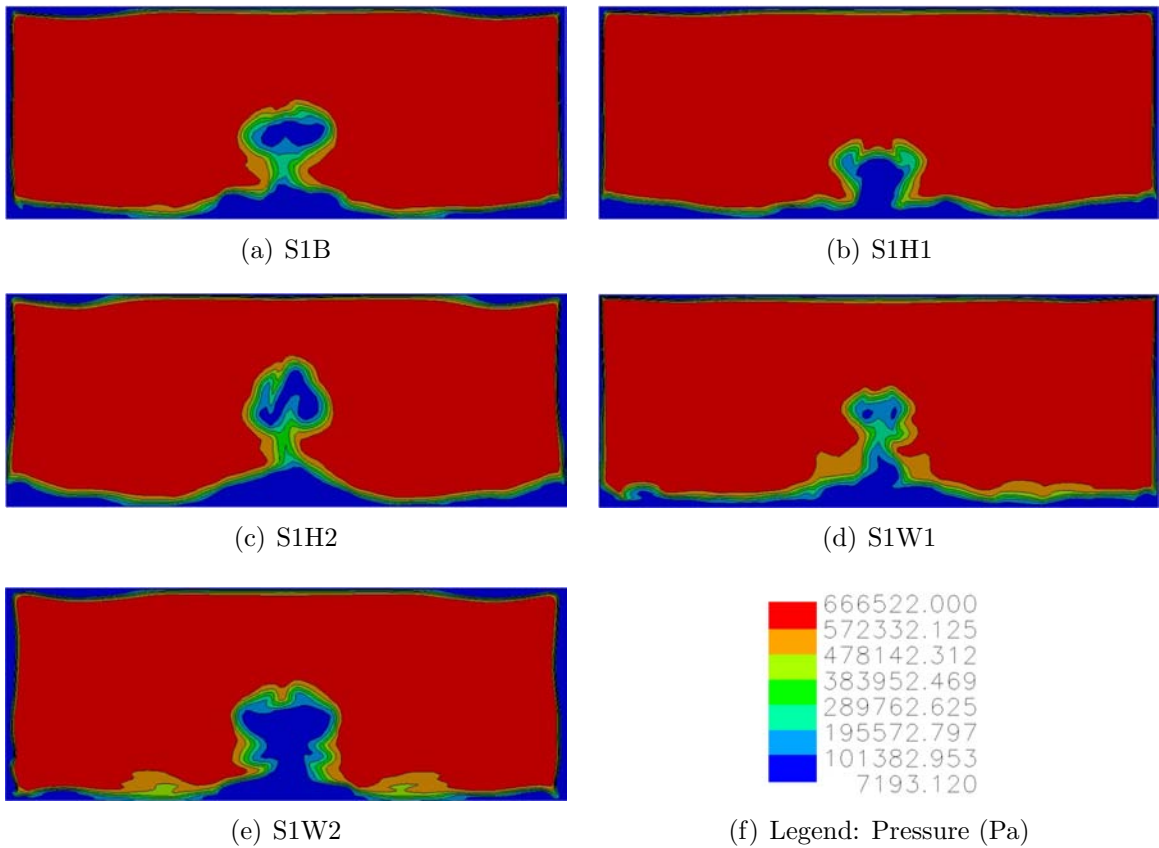


Figure 4.3: Laminar combustion section exit pressure contours

Table 4.2: Turbulent total pressure loss for S1

Strut	P_{in} (Pa)	P (Pa) at 27.94 cm	P at 30.86 cm	P_{out} (Pa)	$\frac{P_{out}}{P_{in}}$
S1B	543368	502298	484708	477136	0.878
S1H1	544289	538402	534038	534038	0.967
S1H2	542975	446357	372643	340818	0.628
S1W1	544563	538230	534985	532502	0.978
S1W2	543871	499667	449602	412805	0.759

the combustion section. The largest total pressure drop typically occurred between the entrance and the first measurement plane. The large drop is caused by the recirculation region just behind the strut and in the cavity. The total pressure contour plots of the total pressure at the exit of the combustion section are shown in Figure 4.4. The total pressure contours at the exit of the combustion section look very similar to the laminar results in Figure 4.3. The strong low pressure region in the middle of S1B, S1H2, and S1W1 is due to the vortex created by the strut. The low total pressure region is less apparent in S1H1 and S1W1 due to the strut shape. In the S1B total pressure contours, there is a larger low pressure region near the walls of the test section. The large low pressure region in the boundary layer is caused by the S1B simulations were able to reach seven orders of magnitude reduction in the residuals, far beyond the required convergence criteria.

In order to take a closer look at what is occurring in the combustion section, velocity profiles were made at the three measurement locations listed in Figure 3.13. The velocity profiles show the evolution of the vortices seen in the exit pressure plot of Figure 4.4. These figures use the same total pressure scale as used in the previous figures. Starting with the velocity fields for S1B in Figure 4.5, two sets of counter rotating vortices are visible. The larger vortices are the pair behind the strut that pull air and fuel from the cavity up the back of the strut. The second set of vortices is created by the top of the strut pulling air from above the strut. Previous research [20] that evaluated a similar shaped strut also looked at the velocity vectors downstream of the strut as shown in Figure 4.6. The image in Figure 4.6 is closer to the back edge of the strut but displays the same four vortices that are seen in this research. Moving

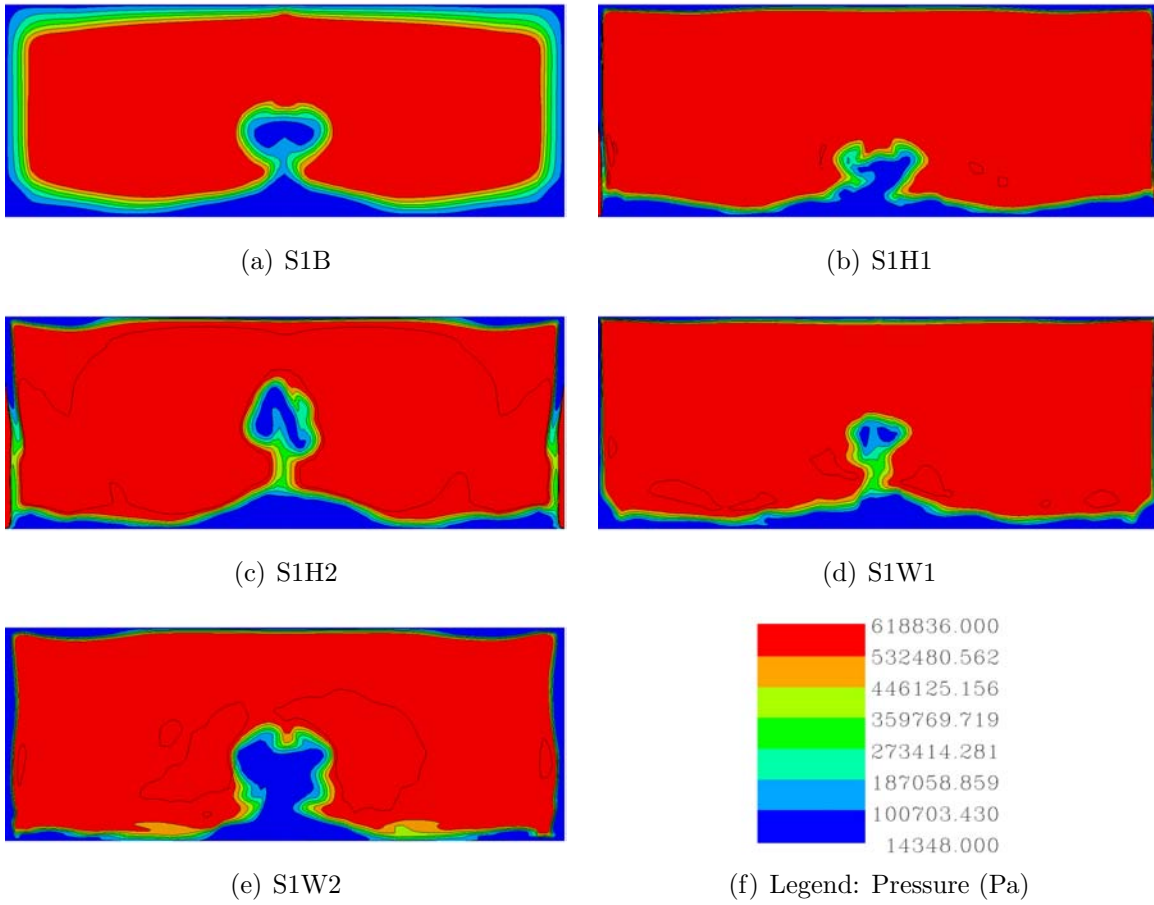


Figure 4.4: Turbulent total pressure contours for S1 at combustion section exit

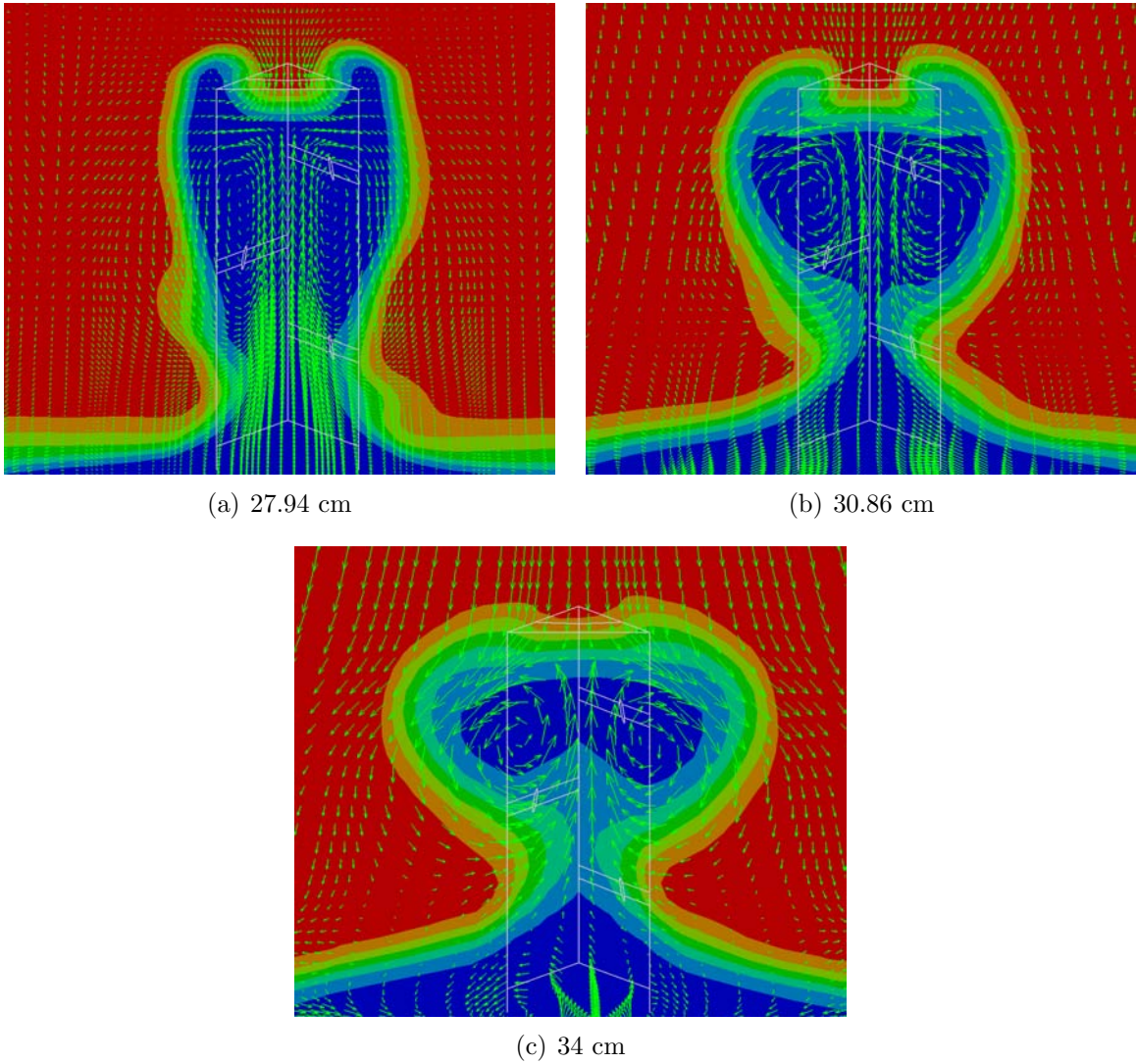


Figure 4.5: Velocity Profiles at different locations after S1B

to the second measurement plane, the larger vortices have increased in strength and nearly eliminated the second set of vortices. At the final measurement plane, the exit of the combustion section, only one set of counter rotating vortices remains which create the low pressure region seen in Figure 4.4.

The velocity profiles for strut S1H1 are displayed in Figure 4.7. At the first measurement plane, only one set of counter-rotating vortices can be seen. The second set that was seen in S1B probably did not form due to the smaller size of S1H1. In the second measurement plane, all four vortices can be seen, but the two from the

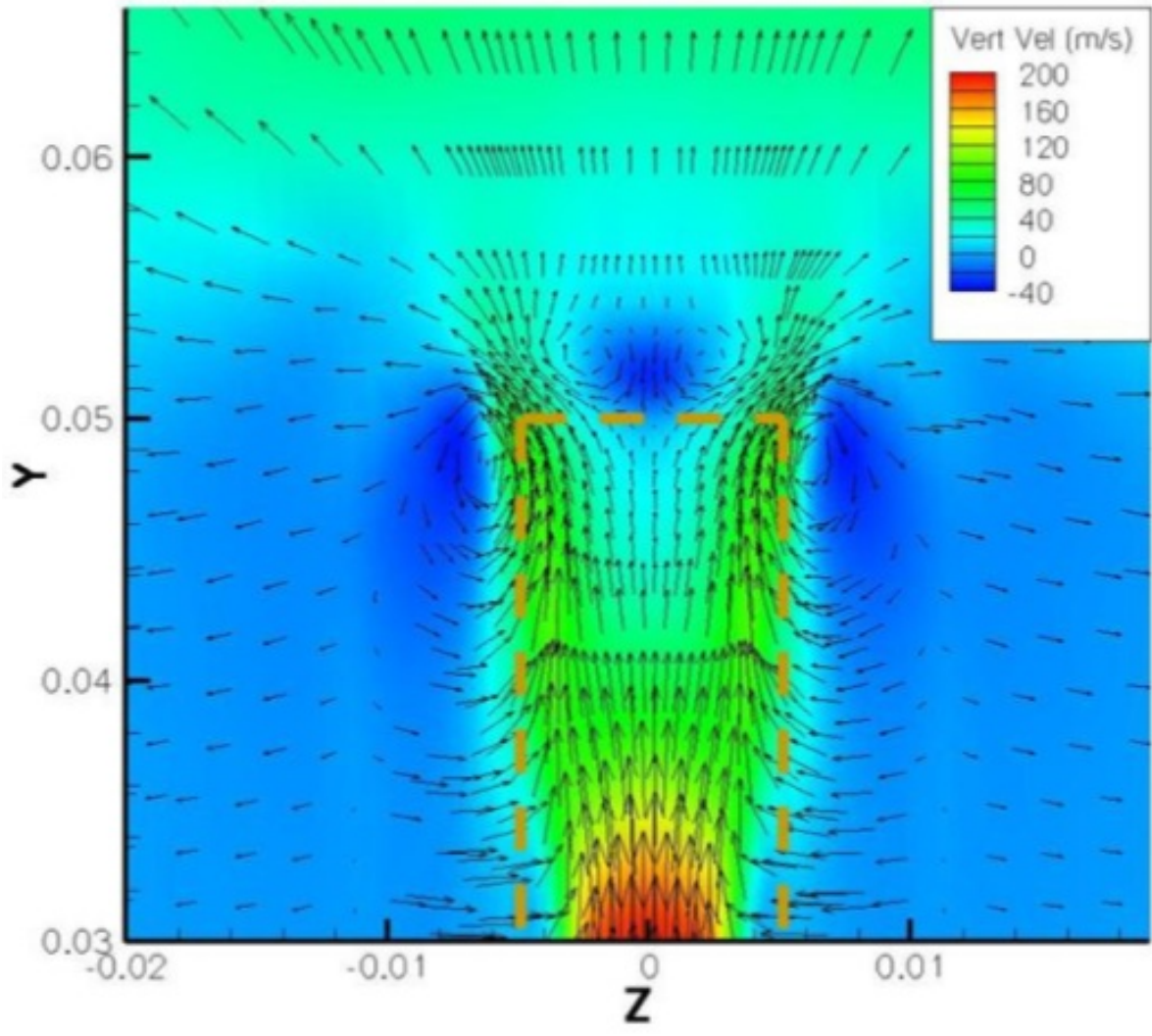


Figure 4.6: Velocity vectors seen in previous research [20]

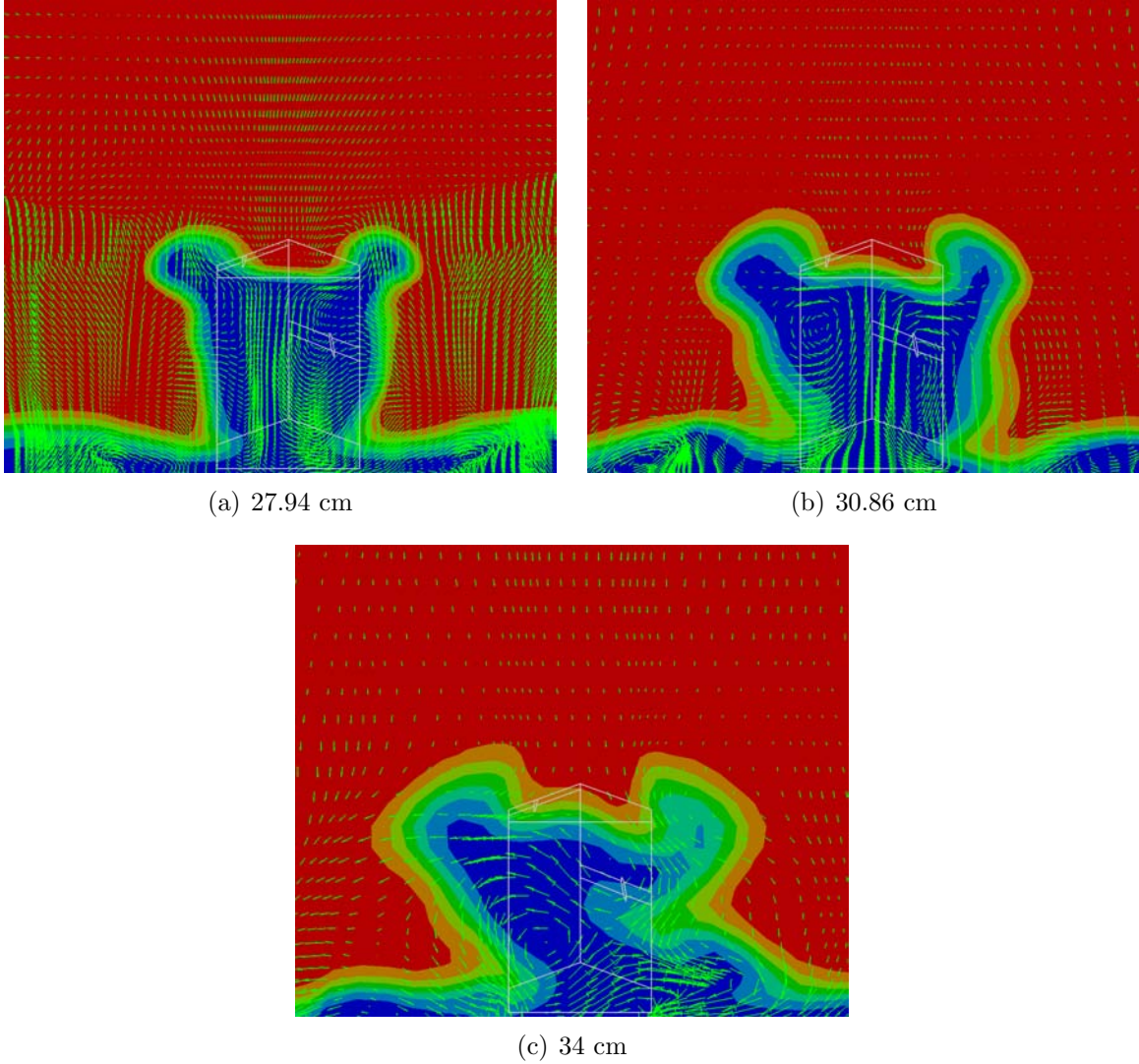


Figure 4.7: Velocity Profiles at different locations after S1H1

top of the strut appear much weaker than the two that form behind the strut. At the exit of the combustion section, there is only one large vortex in the image. It appears that the second vortex of the pair interacted with the cavity and is seen in the bottom right of the image. This asymmetry could be caused by the limited area for the vortices to form behind the strut.

Strut S1H2 has an interesting image at the first measurement plane, as seen in Figure 4.8. A pair of vortices is still formed directly behind the strut, but the vortices that have formed at the top of the previous struts are not present. The lack of the tip

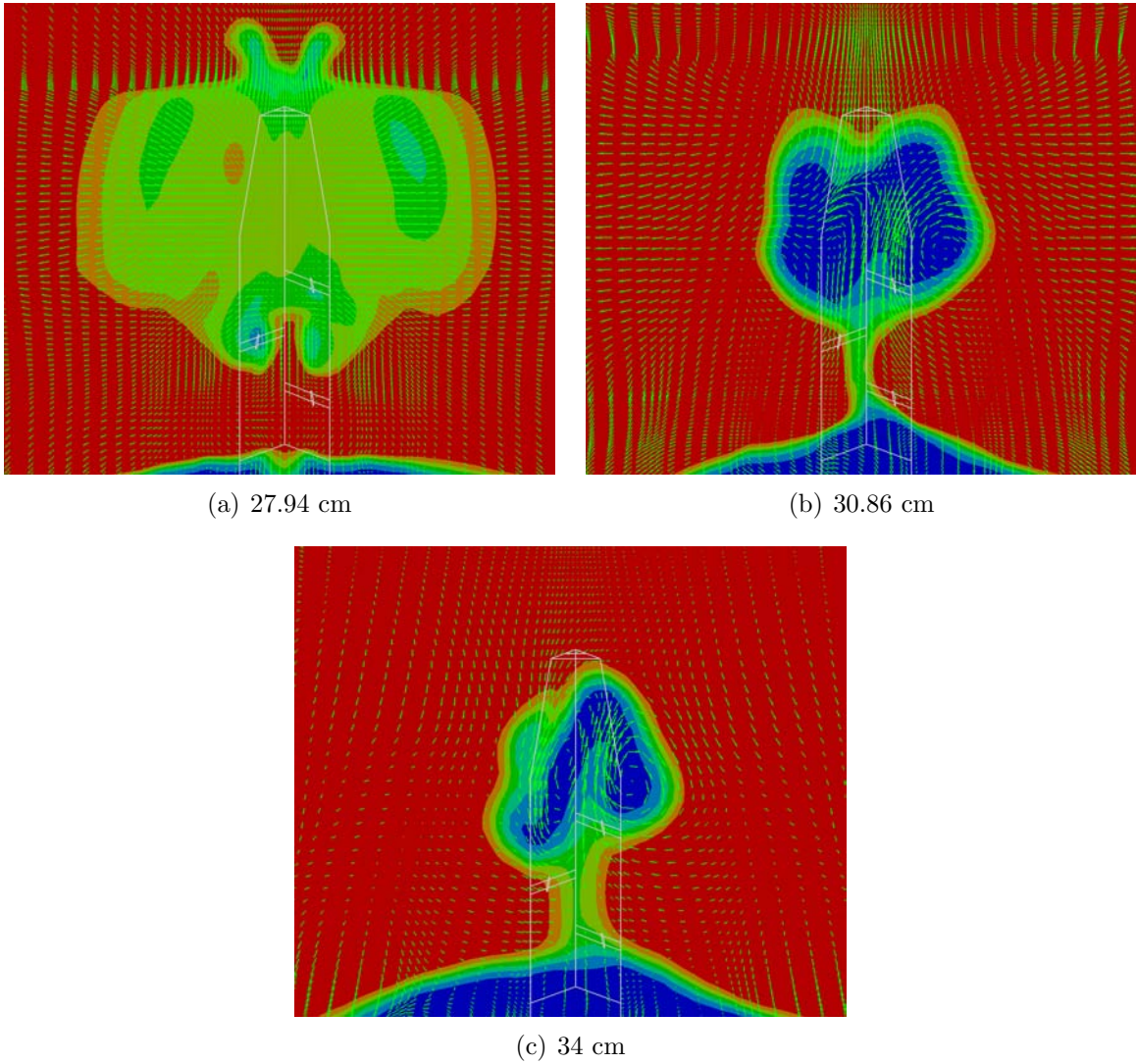


Figure 4.8: Velocity Profiles at different locations after S1H2

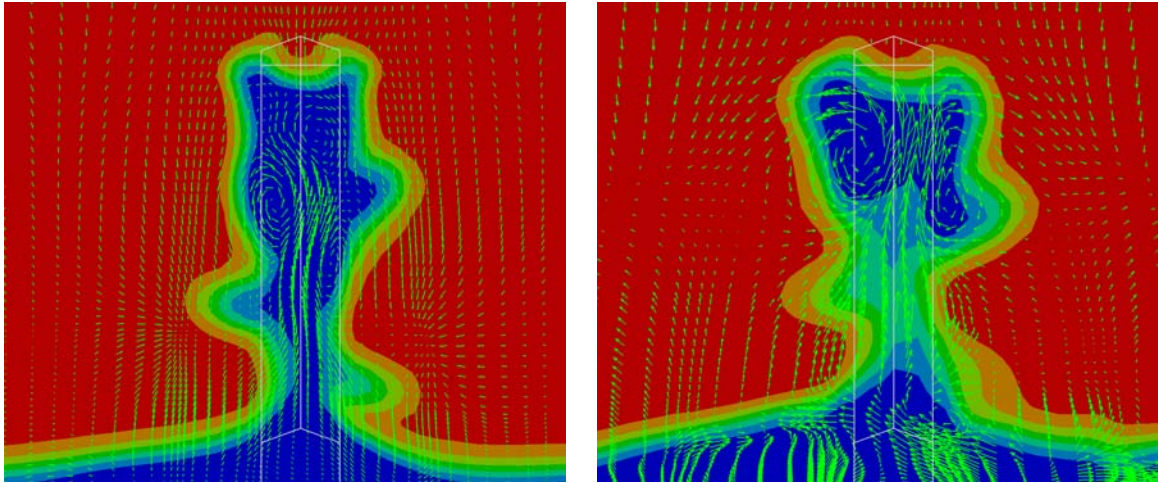
vortices is most likely due to the smaller size of the top of the strut. Since the top of the strut is thinner the vortices were not as strong as those seen on previous struts. The images of the second and last measurement plane appear similar to those of S1B in that only two counter-rotating vortices are seen. In the final image the vortices look stretched. This could be caused by the smaller area of the top of S1H2 and the main flow's effect on the vortices.

In the velocity profile for strut S1W1, Figure 4.9, three vortices are seen on the first measurement plane. As with S1H2, there are no vortices at the top of the strut

due to the smaller size. The three vortices that do appear are arranged so that flow is traveling up the back centerline of the strut and are offset similar to the location of the strut injector ports. In the second measurement plane, two of the vortices have paired near the top of the strut as seen in the earlier struts, while the third has moved toward the cavity. The beginning of a fourth vortex appears to be occurring opposite of the lower vortex. At the exit of the combustion cavity, two vortices are counter rotating at the top of the strut while on the bottom another set is loosely formed. The bottom vortices are counter rotating, but the right vortex is stronger and hindering the formation of the left vortex.

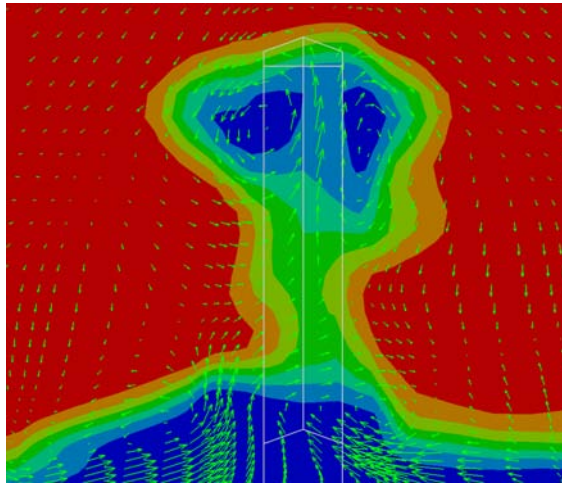
In Figure 4.10, the velocity profiles for strut S1W2 are shown. In the first image, two counter-rotating vortices are seen near the bottom of the strut. Due to the large size of the top of S1W2, another set of vortices were expected at the top of the strut. In the image, there are two low total pressure regions that are a sign of a vortex but the velocity vectors do not confirm them. The lobes on the right and left side of the image may be caused by the fuel injection. In the second image, a third vortex has formed near the top of the strut on the left side. It appears that a fourth vortex is beginning to form opposite the third, but the change in the flow field caused by the top fuel injector on the right side may be hindering the vortex generation. At the exit of the combustion section there is one large vortex on the right and a small vortex on the left side. The one strong vortex may be due to the dual fuel injectors on the right side.

In the first images of Figure 4.8 and 4.10, low total pressure lobes appear on either side of the strut. These lobes disappear in the later images. Streamlines were created that passed through these lobes in an attempt to identify the cause. Figure 4.11 shows the two images including the stream lines. All 12 stream lines end on the surface of the strut. Since the streamlines end in the boundary layer of the strut, the lobes are probably caused by the cells that were limited to the minimum or maximum temperature on the surface of the strut. The point at which the streamlines end are in cells that are limited by the minimum temperature. The cell shape does



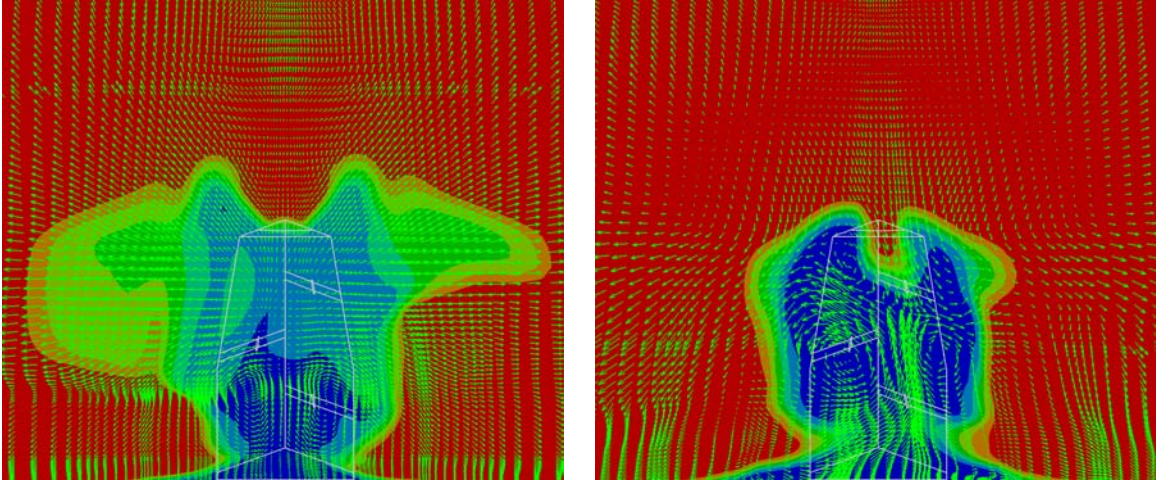
(a) 27.94 cm

(b) 30.86 cm



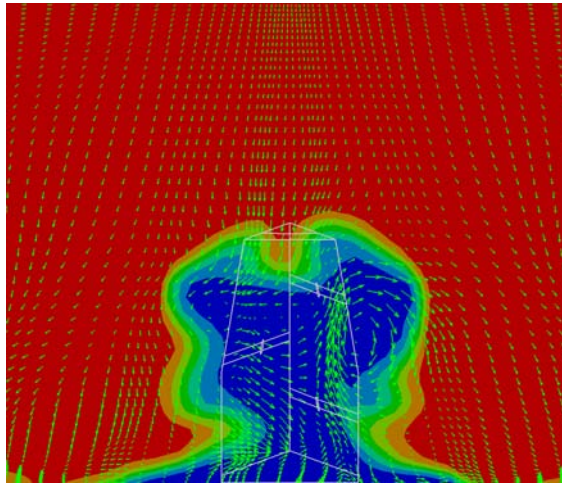
(c) 34 cm

Figure 4.9: Velocity Profiles at different locations after S1W1



(a) 27.94 cm

(b) 30.86 cm



(c) 34 cm

Figure 4.10: Velocity Profiles at different locations following S1W2

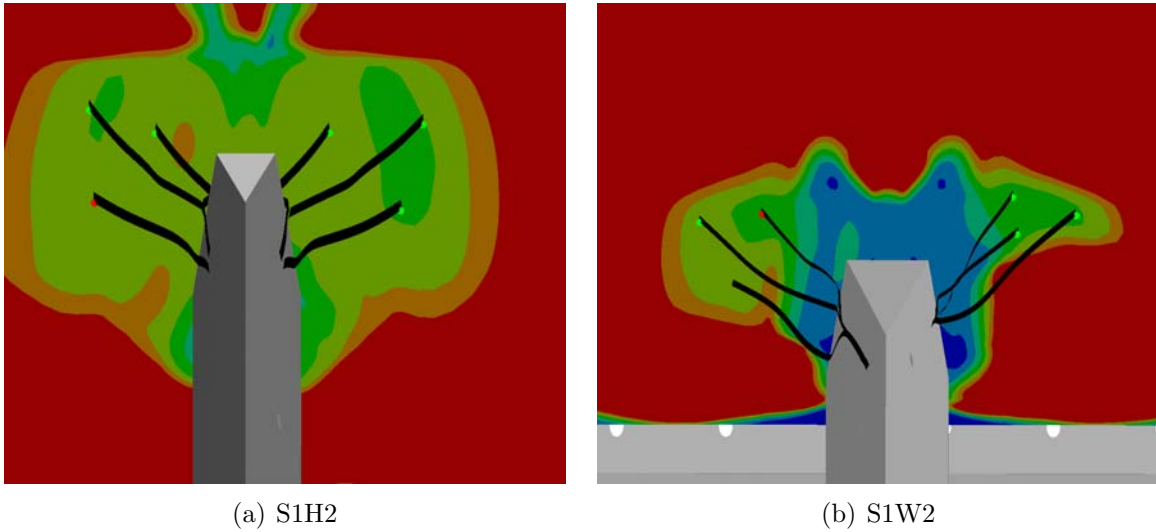


Figure 4.11: Streamlines to identify source of low pressure lobes

not seem to be a contributor to this error since the cells are only slightly skewed similar to those seen in Figure 3.10. The lobes are created by these extremes and then disappear as the flow mixes with the main flow which is why the lobes are not visible in the later images.

While S2B had trouble with the turbulent transitions, as previously discussed, preliminary results support the trends from strut S1 and the laminar results, as shown in Table 4.3. S2B had the lowest total pressure loss since it matches one of the convergence criteria while the other four simulations still require more iterations to reach the set criteria. Total pressure loss data was not collected at intermediate points in the combustion section since these simulations need more iterations to reach a converged state. Velocity vector fields were generated for S2B, S2H2 and S2W2, but only at the second and third measurement planes since the extension of strut S2 crosses the first measurement plane. The background total pressure contours used in the velocity figures uses the same scale as Figure 4.4.

Figure 4.12 shows the velocity vectors at two measurement planes downstream of strut S2B. The first image shows two counter-rotating vortices that formed near the mid section of the strut. In the second image the vortices have moved into a

Table 4.3: Preliminary turbulent total pressure loss for S2

Strut	P_{in} (Pa)	P_{out} (Pa)	$\frac{P_{out}}{P_{in}}$
S2B	551356	521435	0.946
S2H1	549852	416739	0.758
S2H2	545304	345142	0.633
S2W1	551194	415551	0.754
S2W2	546385	334653	0.612

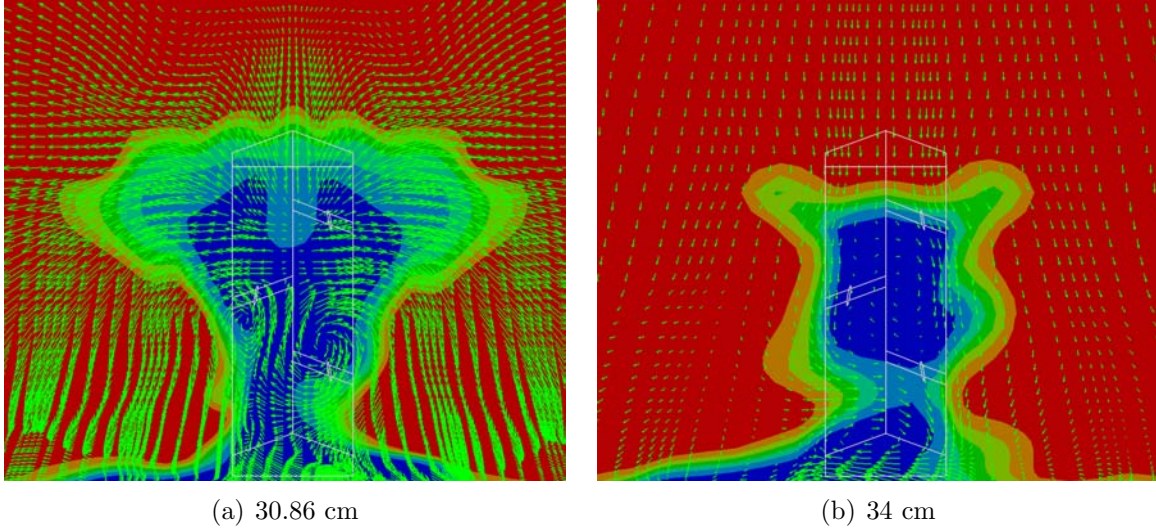


Figure 4.12: Velocity Profiles at two locations following S2B

vertical configuration. In the second configuration, the top vortex is entraining air from above the strut while the lower vortex is pulling up flow from the cavity. While this is preliminary data, this configuration may increase mixing when compared to S1B.

The velocity vector fields for strut S2H2 are shown in Figure 4.13. The velocity vectors in the first image show five vortices behind the strut and two more on either side. The two side vortices may be caused by the high velocity and pressure flow from upstream entering the low velocity and pressure cavity. Since the trailing edge of the S2 struts is slanted at a 45 degree angle, it would promote the creation of these vortices more than the flat trailing edge of S1 struts. The multitude of vortices in the first image become four elongated vortices in the second image at the exit of the combustion section. The bottom set of vortices draw the flow from the cavity up the

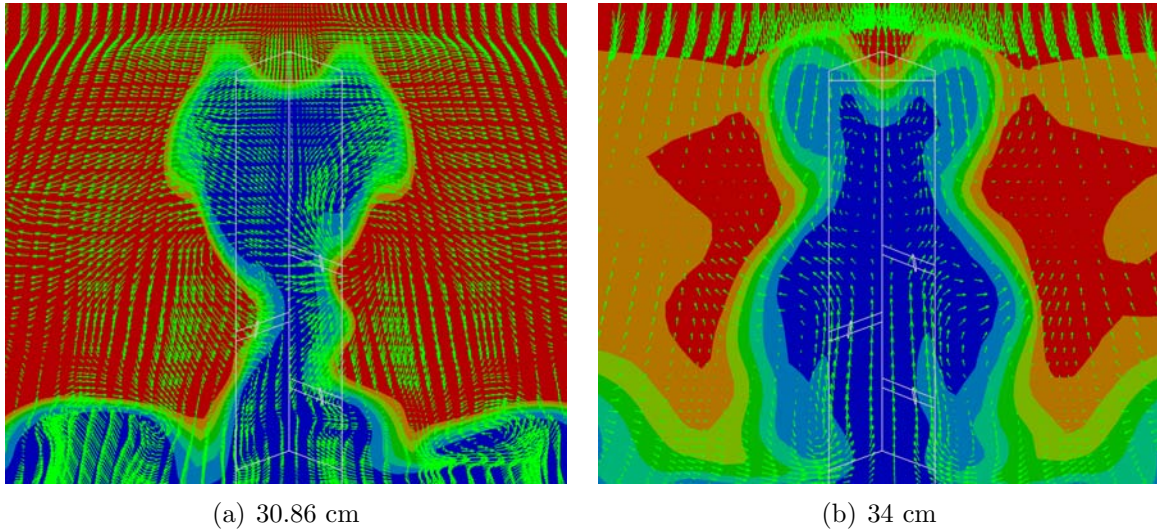


Figure 4.13: Velocity Profiles at two locations following S2H2

back face of the strut while the top pair pull air from above the strut down. While this configuration of vortices may lead to increased mixing, it occurs at the exit of the cavity when it would be preferred if the peak combustible area was reached before the exit.

In the velocity vector images for strut S2W2, found in Figure 4.14, four vortices are visible. Two of the vortices occur near the bottom of the strut similar to those seen with strut S2H2, caused by the interaction of the main flow with the cavity flow. Two more vortices are found near the midsection of the strut similar to S2B. It appears that two more vortices may have existed off the top of the strut, but have degraded at this point in the flow field. In the second image, two vortices appear just below the top of the strut. The wide distance between the two vortices allow flow from above the strut to travel down the back of the strut unlike other struts where flow mostly travel up the back of the strut.

The preliminary results from S3 again re-enforce the trend that the size of the strut is the main factor in the total pressure loss as shown in Table 4.4. Since strut S3B is close to the convergence criteria, velocity fields were generated and can be found in Figure 4.15. Only two images appear in the figure since the first measurement plane

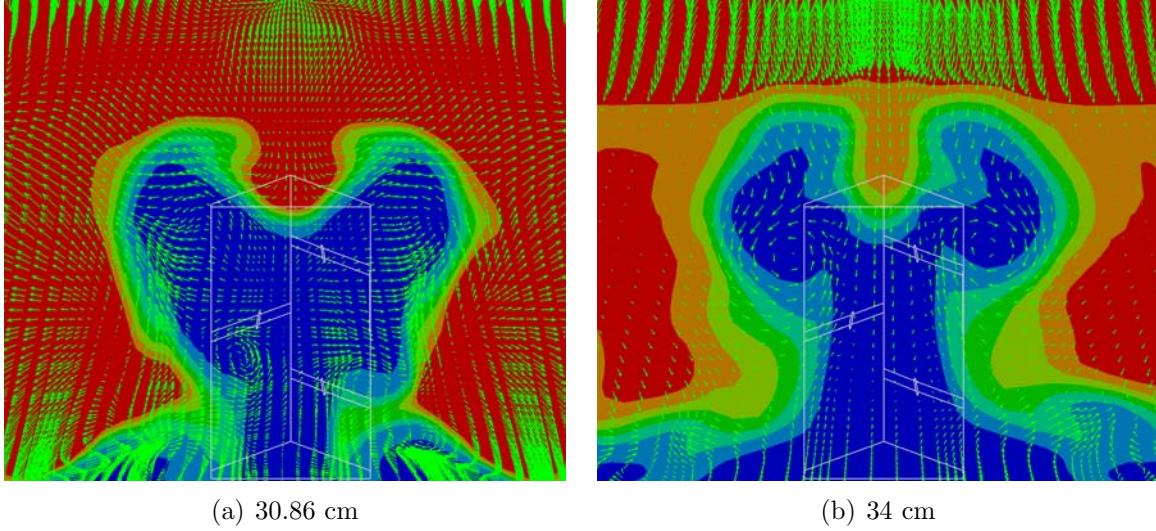


Figure 4.14: Velocity Profiles at two locations following S2W2

Table 4.4: Preliminary turbulent total pressure loss for S3

Strut	P_{in} (Pa)	P_{out} (Pa)	$\frac{P_{out}}{P_{in}}$
S3B	541567	512331	0.946
S3H1	537397	385777	0.718
S3H2	539821	318211	0.589
S3W1	546730	406040	0.743
S3W2	534873	333757	0.624

intersects the extension of the strut and the total pressure contours use the same scale as in Figure 4.4. In the first image, two counter rotating vortices can be seen. The right vortex is between the two strut fuel injectors and the left vortex is just above the left fuel injector. As with previous velocity profiles the vectors show flow moving from the cavity up the back of the strut. In the second image, four vortices are shown. The four vortices occur between the strut fuel injectors and are possibly re-enforced by the fuel injection. This configuration of vortices is similar to the first image in Figure 4.5. Due to the extension of S3B, these two images should look similar since they both occur at the same distance behind the back of the strut.

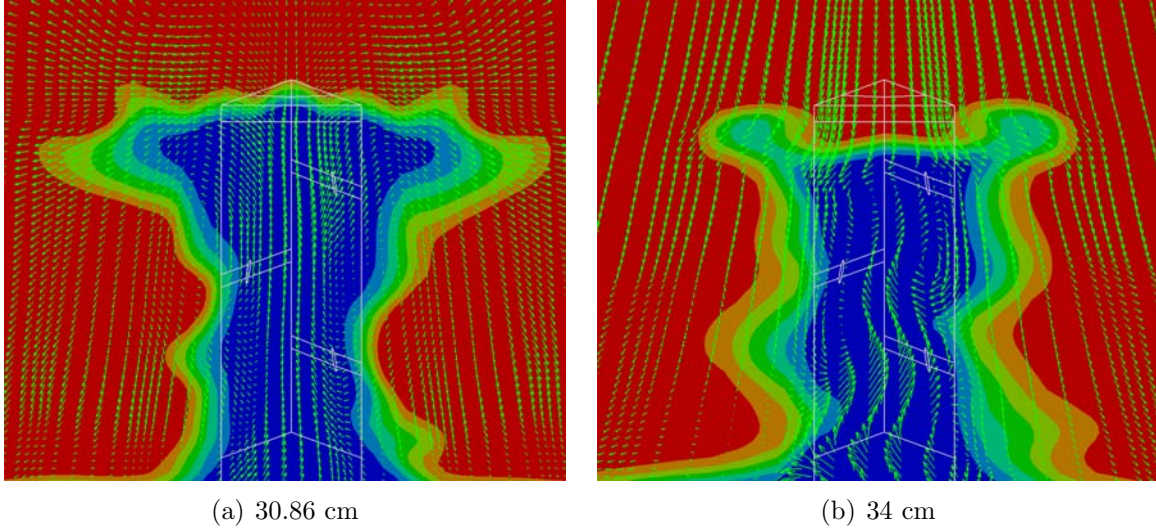


Figure 4.15: Velocity Profiles at two locations following S3B

4.2 Combustible Area

As with the total pressure loss, the combustible area is expected to be related to the size of the strut due to the recirculation region illustrated in Figures 4.1 and 4.2. Larger struts, W2 and H2, are expected to have a larger combustible area than H1 and W1 struts. The combustible area is calculated by using limit on the equivalence ratio as defined in Chapter 3.

4.2.1 Laminar. The combustion area at each measurement plane for each of the struts is found in Table 4.5, and can be visually seen in Figure 4.16. S1H1 has the smallest mixing area at each location. Combining this observation with the earlier result of S1H1 having the lowest total pressure drop a connection can be made between the amount of pressure ratio and the combustion area. The connection between the pressure loss and combustion area also holds for the two larger struts, S1H2 and S1W2. The outlier is S1W1.

S1W1 had a lower total pressure loss but also had a larger combustion area than all of the other struts at the first and second measurement locations. Both of these locations are in the combustion cavity and would add to the combustion in the combustion section. An explanation for this difference is that the fuel injectors on

Table 4.5: Combustion area (cm²) at three locations behind the strut

	Location (cm)		
Strut	27.94	30.86	34
S1B	1.706	2.871	5.668
S1H1	1.582	2.510	3.945
S1H2	2.784	4.616	6.838
S1W1	3.864	5.149	4.517
S1W2	1.635	3.374	6.964

S1W1 are on the flat face of the strut, injecting perpendicular to the flow and not on the wedge face. With the injectors after the wedge face, they would be in an area of lower pressure and velocity due to the expansion wave caused by the geometry of the strut. The lower pressure and velocity would give the fuel from the strut injectors more penetration into the flow. Even though this is not a turbulent case, a shear layer would be present that would increase the mixing of the air and fuel.

4.2.2 Turbulent. The combustible area for the turbulent results of S1 are shown in Table 4.6 and are shown graphically in Figure 4.17. For most of the results, the turbulent combustible area is larger than the laminar combustible area as was expected due to the increased mixing caused by turbulence. The combustible area results show that S1H2 and S1W2 have the larger combustible areas at most stations. The larger combustible area of S1W2 and S1H2 were expected due to the larger size of the strut. S1H1 and S1W1 have the lowest combustible area at each station. It is interesting to note that the odd S1W1 result from the laminar case does not exist once turbulent simulations were completed. The size of the strut was expected to be the major contributor to the combustible area and that trend was upheld by these results. In S1H1, S1H2 and S1W2, the combustible area decreases or fluctuates through the combustion section. The change in combustible area seen in S1H1, S1H2 and S1W2 are probably due to an attempt to run reacting flow calculations in these simulations. The reacting flow would have combusted a portion of the fuel causing the fluctuation in the combustible area. For S1H2 and S1W2, the lobes seen in Figure 4.8 and 4.10 have caused the increase in the initial combustible area calculations. While these

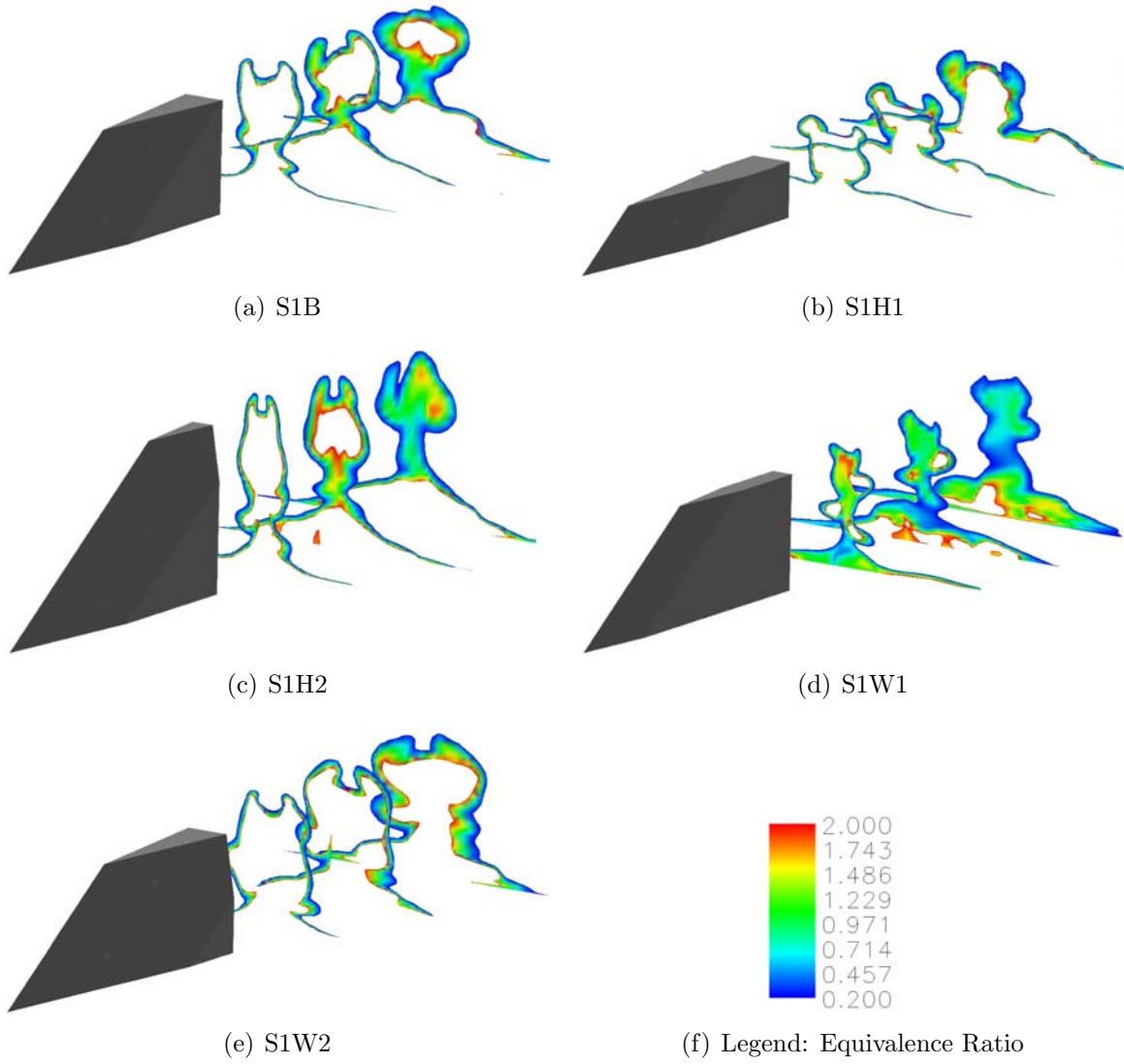


Figure 4.16: Laminar equivalence Ratio at three stations behind the strut

Table 4.6: Combustion area (cm²) at three locations behind S1

	Location (cm)		
Strut	27.94	30.86	34
S1B	2.996	6.029	10.14
S1H1	3.313	2.919	4.035
S1H2	12.588	9.546	7.379
S1W1	1.642	4.668	6.175
S1W2	6.457	5.409	7.29

Table 4.7: Preliminary Combustion area (cm²) for S2 and S3B

	Location (cm)		
Strut	27.94	30.86	34
S2B	6.892	3.693	6.54
S1H2	2.224	2.017	1.562
S1W2	1.224	3.68	1.0567
S3B	6.977	3.811	4.942

lobes have introduced error into the combustible area calculation, it is believed that even without the lobes these two struts would create a larger combustible area as supported by the laminar data.

The preliminary combustible area for strut S2B, S2H2 and S2W2 are shown in Table 4.7. The combustible area for S2B fluctuates through the combustion section. The preliminary combustible area for strut S3B is included in Table 4.7. Strut S3B is currently the only S3 strut that has run enough iterations for the fuel to have reached the cavity of the combustion section but not enough to reach convergence. The preliminary measurements of combustible area show a steady decrease throughout the combustion section. Since the combustible area decreases against the trends shown on the other struts, more iterations are required for the mixing flow field to develop to allow more accurate measurements.

4.3 Flame Comparison

While the simulation did not involve reactions, an estimation of the flame location was created by using an iso-surface of C₂H₄ and the equivalence ratio as a limiter.

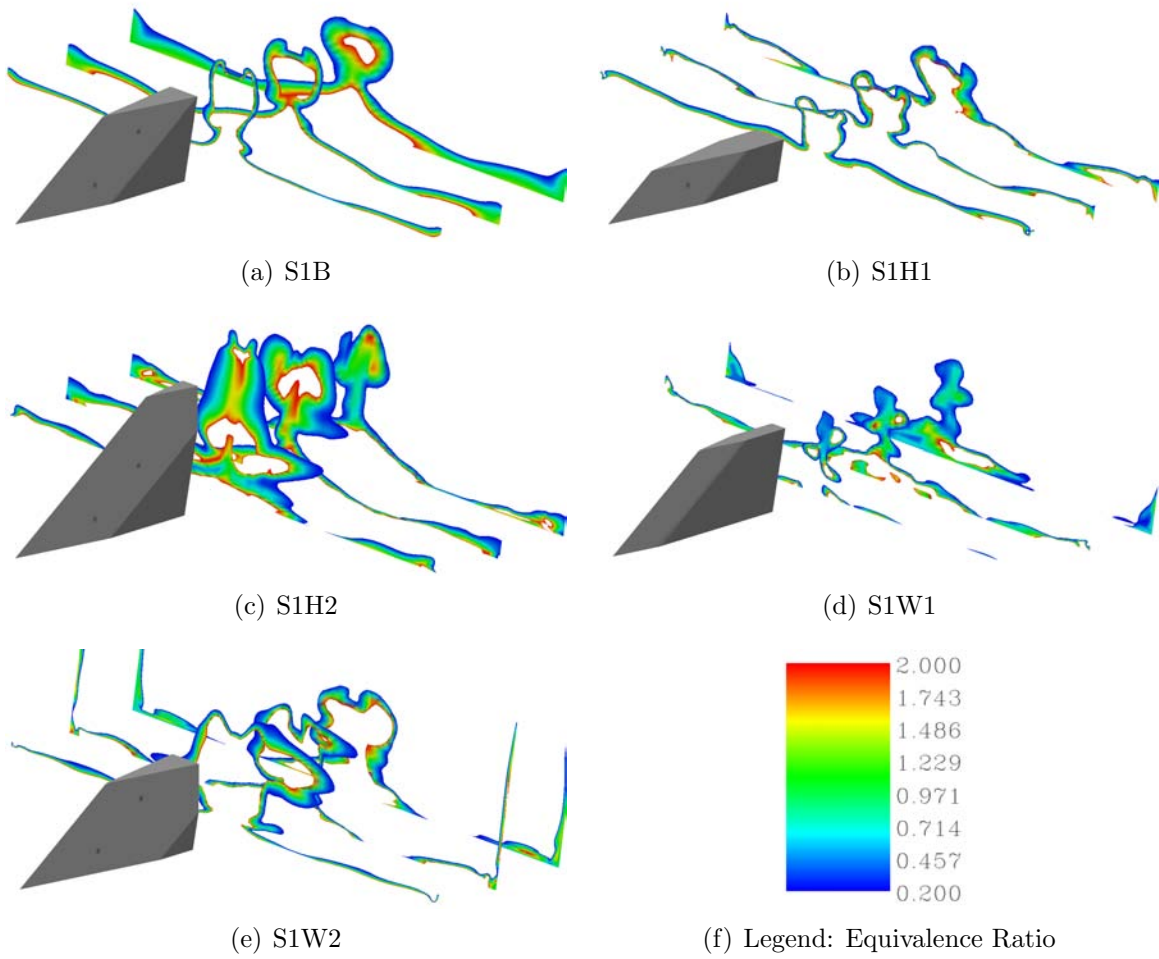


Figure 4.17: Equivalence ratio at three stations behind strut S1

Using the iso-surface allows a visualization of where the flame can occur, but does not factor in the burning of the fuel, so the computational images over-estimate the flame zone and show possible flame upstream of the cavity. Figures 4.18 through 4.20 show a comparison between the computational flame location and the experimental flame location. For strut S1B, the computational and experimental [4] flame images look similar as seen in Figure 4.18. Both images show combustion in the cavity and near the top of the back edge of the strut. The combustion near the top of the strut is caused by the recirculation region and the vortex shed off the top of the strut. Figure 4.19 shows the comparison between computational and experimental flame images for S2B. While S2B does not show as good a comparison as S1B, the general shape is consistent. The computational flame images shows more separation between S2B and the start of the flame while the experimental image shows only a small gap. As with the previous struts, the images for S3B have similar structures and can be seen in Figure 4.20. In both images of S3B's flame image, there is a flame starting at the center of the back of the strut that flows toward the top of the strut as it moves downstream. In the S3B computational image, some of the flame zone in the cavity was removed to get a better look at the flame just behind the strut, which is why there is not flame along the side of the strut in the cavity.

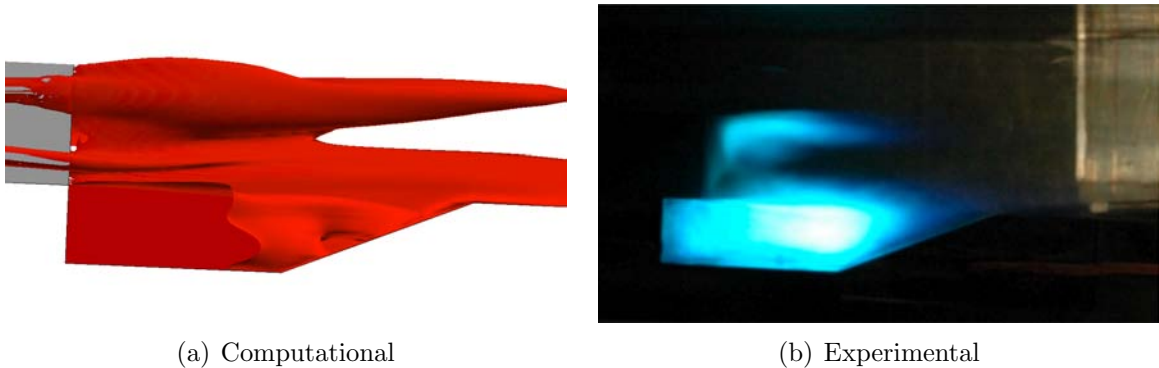
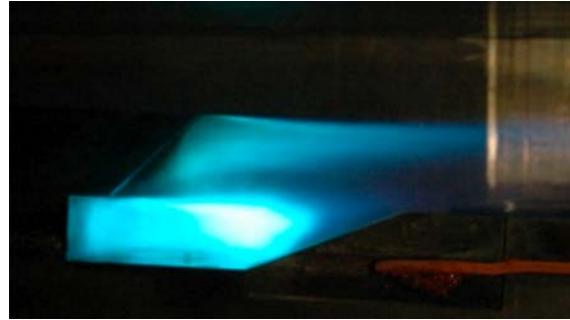


Figure 4.18: Flame location for S1B



(a) Computational

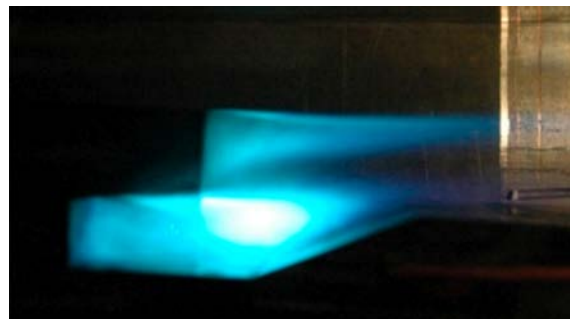


(b) Experimental

Figure 4.19: Flame location for S2B



(a) Computational



(b) Experimental

Figure 4.20: Flame location for S3B

V. Conclusions

Interest in enhanced propulsion capabilities for Scramjet engines has increased in recent years for hypersonic vehicles required for rapid space access. The difficulty for scramjet engines is the mixing and combustion of fuel without the need for a large combustion chamber. To combat a large combustion chamber, several different mixing enhancement techniques have been evaluated. Using a mixing enhancement technique in a scramjet could lead to smaller scramjets that would reduce the total weight of any vehicle it is used on. A strut is one mixing enhancement technique that has the ability to affect the entire flow in the combustion section. Struts have been used for many years to inject fuel and increase the mixing for combustion.

This research focused on a parametric study of the geometry of the struts used for fuel injection to determine trends in the fuel mixing caused by variations in the height and width of the struts. Three strut designs with different trailing edge shapes were used as baselines. Each of the strut designs had the height and width increased or decreased by 50% of the baseline value to create a total of fifteen struts. Except for the height and width all other geometry parameter remained constant. Each strut geometry was evaluated on two parameters key to scramjet combustion sections; the total pressure loss and the combustible area.

The total pressure loss caused by the combustion section of the scramjet is a key measure of the efficiency of the engine. To evaluate the total pressure, the area average total pressure was collected on a constant plane normal to the flow direction. The average total pressure was collected at four locations; just before the strut placement, two locations in the combustion cavity and at the exit of the combustion section. Comparing the total pressure at these planes, it was found that the total pressure drops through the combustion section, the largest total pressure loss occurring early in the combustion section. The increased total pressure loss at the early measurement location is caused by the recirculation region created behind the struts. The recirculation region allows fuel and air from the cavity to flow up the back side of the strut and mix with the main flow in the combustion section. The

larger struts, the struts with increased height or width, displayed the largest total pressure loss across all strut designs. The larger struts create a larger recirculation region behind them causing the increased total pressure loss. The smaller struts, with decreased height or width, showed a lower total pressure loss due to the smaller recirculation region created.

The velocity profiles were examined at the same location as the total pressure except for the measurement plane just before the strut. At the first measurement location the velocity field showed at least two counter rotating vortices and as many as four vortices behind the strut. The typical two vortex structure occurred near the middle or lower part of the strut in the recirculation region. The second set of vortices were created by the top of the strut. The tall and thin strut did not produce as strong of a set of vortices off the top of the strut due to their smaller size of the top. The short struts created the pair of vortices off their top sooner than the vortices in the recirculation region due to the smaller area for the recirculation region. As the flow traveled through the combustion section, the number of vortices decreased. In most cases at the exit of the combustion section, there were two counter rotating vortices that dominated the flow field. The vortices are key to mixing the fuel and air to the point where it is combustible.

The combustible area was calculated at the same three planes where velocity data was collected. To find the combustible area, the equivalence ratio was calculated at each plane. The equivalence ratio compares the mixture of fuel and air to the ideal fuel and air mixture and combustion was assumed to occur between an equivalence ratio of 0.2 to 2. In general the combustible area increased from the first measurement plane to the exit of the combustion section. Some of the struts had a slight decrease of the combustible area in the second measurement plane. The decrease could be caused by the break down of vortices that temporarily decreases the mixing that occurs at that location. On average, the tall and wide struts generated a larger combustible area than the short and thin struts. As with the total pressure loss,

the larger recirculation region generated by the tall and wide struts allows for more mixing to occur and therefore a larger combustible area.

While no conclusive data was collected comparing the effect of the three different trailing edge designs, the placement and size of the recirculation region behind the strut was a major factor in the performance. Since two of the trailing edge designs intrude over the combustion cavity, this would reduce the area the recirculation region has to form. Since the flat trailing edge design allows for the recirculation region to form sooner, it appears to be the better design to increase mixing and performance of the scramjet.

This research evaluated a variety of strut geometries and the effect on key performance parameters for the combustion section of a scramjet engine. This work determined the relationship between the total pressure loss and combustible area with variations in the height and width of the strut in a steady state, viscous, turbulent and non-reacting computational simulation. The connection between the strut shape and the performance of the combustion section is critical information for the use in design tradeoffs when developing the layout of the combustion section of a scramjet engine.

5.1 Impact

This paper provides information that can be used as a foundation for future research into strut design in a combustion section. The results identify relationships in mixing and performance due to different strut geometries. While the larger struts caused a larger total pressure loss the increase in combustible area may balance the loss of efficiency. The balance between the total pressure loss and combustible area would become a primary design tradeoff for future strut designs. The results of this research suggest that strut 1 baseline is the best starting point for a strut design

5.2 Future Work

Due to the complexity of these simulations and the issues encountered in transitioning from laminar to turbulent calculations a limit was reached on computational resources and time. Continuing the simulations used in this research would lead to more accurate and clear comparison between all fifteen test cases. Also, the addition of reaction equations in the VULCAN solver would allow the simulations to better match the experimental results and allow for thrust to be used as a key parameter.

Using these results, it would be interesting to evaluate an array of multiple struts which would be more indicative of a real world scramjet engine. Using the different strut designs and different distances would allow for the evaluation of the effect the struts would have on each other and the combustion section of the scramjet.

The flat back edge of the struts used in this research created a strong recirculation region which was the primary cause of total pressure loss. It would be interesting to see if a diamond shaped strut similar to those used in previous NASA research [16] would cause comparable mixing while decreasing the total pressure loss.

Bibliography

1. E. T. Curran, "Scramjet engines: The first forty years," *Journal of Propulsion and Power*, vol. 17, no. 6, pp. 1138 – 1148, 2001.
2. E. T. Curran and S. N. B. Murthy, eds., *Scramjet Propulsion*, vol. 189 of *Progress in Astronautics and Aeronautics*. American Institute of Aeronautics and Astronautics, 2000.
3. F. S. Billig, "Two-dimensional model for thermal compression," *Journal of Spacecraft and Rockets*, vol. 9, no. 9, p. 702, 1972.
4. K. Y. Hsu, C. D. Carter, M. R. Gruber, and T. Barhorst, "Experimental study of cavity-strut combustion in supersonic flow," AIAA Paper 2007-5394, Air Force Research Lab, 2007.
5. Wikipedia, "Scramjet," 2009.
6. P. Waltrup, "Upper bounds on the flight speed of hydrocarbon-fueled scramjet-powered vehicles," *Journal of Propulsion and Power*, vol. 17, no. 6, pp. 1199–1204, 2001.
7. J. C. Hermanson and P. E. Dimotakis, "Effects of heat release in a turbulent reacting shear layer," *Journal of Fluid Mechanics*, vol. 199, pp. 333–375, 1989.
8. J. P. Drummond, *Numerical Simulation of a Supersonic Chemically Reacting Mixing Layer*. PhD thesis, George Washington University, 1987.
9. M. P. Lee, B. K. McMillin, J. L. Palmer, and R. K. Hanson, "Two-dimensional imaging of combustion phenomena in a shock tube using planar laser-induced fluorescence," AIAA Paper 91-0460, AIAA, 1991.
10. P. E. Dimotakis, "Turbulent free shear layer mixing and combustion," *High Speed Flight Propulsion Systems*, vol. 137, 1991.
11. S. D. Stouffer, N. R. Baker, D. P. Capriotti, and G. B. Northam, "Effects of compression and expansion ramp fuel injector configurations on scramjet combustion and heat transfer," AIAA Paper 93-0609, AIAA, 1993.
12. O. Dessornes and C. Jourdain, "Mixing enhancement techniques in a scramjet," AIAA Paper 1998-1517, ONERA, 1998.
13. T. Sunami, M. N. Wendt, and M. Nishioka, "Supersonic mixing and combustion control using streamwise vortices," AIAA Paper 1998-3271, National Aerospace Laboratory, 1997.
14. T. Sunami, P. Magre, A. Bresson, F. Grisch, M. Orain, and M. Kodera, "Experimental study of strut injectors in a supersonic combustor using oh-plif," AIAA Paper 2005-3304, JAXA and ONERA, 2005.

15. Desikan.S.L.N and J. Kurian, "Mixing studies in supersonic flow employing strut based hypermixers," AIAA Paper 2005-3643, Indian Institute of Technology, 2005.
16. L. A. Povinelli, "Aerodynamic drag and fuel spreading measurements in a simulated scramjet combustion module," NASA Technical Note TN D-7674, NASA, 1974.
17. R. A. Baurle, *VULCAN Users Manual*. NASA HAPB, 2008.
18. J. Blazek, *Computational Fluid Dynamics: Principles and Applications*. Elsevier, 2005.
19. J. D. Mattingly, W. H. Heiser, and D. T. Pratt, *Aircraft Engine Design*. American Institute of Aeronautics and Astronautics, 2002.
20. A. B. Freeborn, P. I. King, and M. R. Gruber, "Leading edge pylon effects on a scramjet pylon-cavity flameholder flowfield," AIAA Paper 2008-4709, Air Force Institute of Technology, 2008.

Vita

Matthew Guy Bagg was born in Kingston, NY. He graduated from Avon High School in 1999 and attended Purdue University. He graduated from Purdue University in December of 2003 with a Bachelor degree in Aerospace Engineering and entered active duty in the Air Force. His first assignment was at Wright-Patterson AFB, OH as a member of the Air Force Research Lab Air Vehicles Directorate. As a member of the Weapon Integration team he built computational grids for the evaluation of weapon separation from aircraft. In 2006, he transferred to the Computational Science branch of the Air Vehicles Directorate. In the job he developed and tested computational models for small unmanned air vehicles (UAV). Matt was accepted into the Masters program at the Air Force Institute of Technology at Wright-Patterson in 2007.

Permanent address: 2950 Hobson Way
Air Force Institute of Technology
Wright-Patterson AFB, OH 45433

REPORT DOCUMENTATION PAGE			<i>Form Approved</i> <i>OMB No. 0704-0188</i>	
The public reporting burden for this collection of information is estimated to average 1 hour per response, including the time for reviewing instructions, searching existing data sources, gathering and maintaining the data needed, and completing and reviewing the collection of information. Send comments regarding this burden estimate or any other aspect of this collection of information, including suggestions for reducing this burden to Department of Defense, Washington Headquarters Services, Directorate for Information Operations and Reports (0704-0188), 1215 Jefferson Davis Highway, Suite 1204, Arlington, VA 22202-4302. Respondents should be aware that notwithstanding any other provision of law, no person shall be subject to any penalty for failing to comply with a collection of information if it does not display a currently valid OMB control number. PLEASE DO NOT RETURN YOUR FORM TO THE ABOVE ADDRESS.				
1. REPORT DATE (DD-MM-YYYY) 26-03-2009		2. REPORT TYPE Master's Thesis	3. DATES COVERED (From — To) Sept 2007 – March 2009	
4. TITLE AND SUBTITLE Computational Analysis of Geometric Effects on Strut Induced Mixing in a Scramjet Combustor			5a. CONTRACT NUMBER	
			5b. GRANT NUMBER	
			5c. PROGRAM ELEMENT NUMBER	
6. AUTHOR(S) Bagg, Matthew G., Captain, USAF			5d. PROJECT NUMBER	
			5e. TASK NUMBER	
			5f. WORK UNIT NUMBER	
7. PERFORMING ORGANIZATION NAME(S) AND ADDRESS(ES) Air Force Institute of Technology Graduate School of Engineering and Management (AFIT/ENY) 2950 Hobson Way WPAFB OH 45433-7765			8. PERFORMING ORGANIZATION REPORT NUMBER AFIT/GAE/ENY/09-M01	
9. SPONSORING / MONITORING AGENCY NAME(S) AND ADDRESS(ES) Air Force Research Lab Propulsion Directorate Dr. Dean Eklund 1950 Fifth St Bldg 18D Rm D232 Wright-Patterson OH, 45433-7251 937-785-0632			10. SPONSOR/MONITOR'S ACRONYM(S) AFRL/RZ	
			11. SPONSOR/MONITOR'S REPORT NUMBER(S)	
12. DISTRIBUTION / AVAILABILITY STATEMENT APPROVED FOR PUBLIC RELEASE; DISTRIBUTION UNLIMITED				
13. SUPPLEMENTARY NOTES				
14. ABSTRACT In order to increase the fuel-air mixing in a scramjet combustion section, the Air Force Institute of Technology and the Air Force Research lab investigated methods to increase the mixing efficiency. Previous experimental work identified the advantages of using a strut upstream of a cavity flame holder to increase the fuel-air mixture. In this paper a computational investigation of strut injectors in a supersonic flow with a cavity flame holder is reported. This research focused on understanding the effect of a change in height and width of the strut upstream of the combustion cavity on the mixing efficiency and pressure loss in the combustion section. Three baseline struts from the previous experimental research had slightly different trailing edge designs; a flat trailing edge, a 45 degree slanted trailing edge and a 6.45 cm extension. Twelve more struts were made from the baselines struts by varying the height and width by 50% of the baseline value. Computational simulations were conducted on all fifteen struts using the VULCAN computational fluid dynamics solver. Struts with a height or width increased from the baseline value exhibited an increase in the total pressure loss through the combustion section. This total pressure loss correlated to the larger low pressure region created by the flow displacement caused by the strut. The struts evaluated with decreased height and width showed a lower total pressure loss since they produced a smaller low pressure region in the wake. The low pressure region is key to the mixing caused by the struts. The larger struts caused a larger combustible area in the combustion section while the small struts produced a smaller combustible area. The size of the strut becomes a key design tradeoff between increased mixing and total loss performance.				
15. SUBJECT TERMS Mixing, Scramjet, CFD, Strut				
16. SECURITY CLASSIFICATION OF:		17. LIMITATION OF ABSTRACT UU	18. NUMBER OF PAGES 74	19a. NAME OF RESPONSIBLE PERSON Dr. Robert Greendyke Associate Professor
a. REPORT U	b. ABSTRACT U			c. THIS PAGE U